Utah State University

DigitalCommons@USU

5-2018

Three Environmental Fluid Dynamics Papers

Eden Furtak-Cole
Utah State University

Follow this and additional works at: https://digitalcommons.usu.edu/etd

Part of the Mathematics Commons

Recommended Citation

Utah State University
MERRILL-CAZIER LIBRARY

THREE ENVIRONMENTAL FLUID DYNAMICS PAPERS

by

Eden Furtak-Cole

A dissertation submitted in partial fulfillment
of the requirements for the degree

of

DOCTOR OF PHILOSOPHY

in

Mathematics

Approved:

_____   _____
Joeseph Koebbe, PhD   Luis Gordillo, PhD
Major Professor   Committee Member

_____   _____
Michael Cortez, PhD   Brynja Kohler, PhD
Committee Member   Committee Member

_____   _____
Geordie Richards, PhD   Mark R. McLellan, PhD
Committee Member   Vice President for Research and
                                           Dean of the School of Graduate Studies

UTAH STATE UNIVERSITY
Logan, Utah

2017

ABSTRACT

Three Environmental Fluid Dynamics Papers

by

Eden Furtak-Cole, Doctor of Philosophy

Utah State University, 2017

Major Professor: Joeseph Koebbe, PhD
Department: Mathematics and Statistics

Three papers are presented, applying computational fluid dynamics methods to fluid flows in the geosciences. In the first paper, a numerical method is developed for single phase potential flow in the subsurface. For a class of monotonically advancing flows, the method provides a computational savings as compared to classical methods and can be applied to problems such as forced groundwater recharge. The second paper investigates the shear stress reducing action of an erosion control roughness array. Incompressible Navier-Stokes simulations are performed for multiple wind angles to understand the changing aerodynamics of individual and grouped roughness elements. In the third paper, a 1D analytical flow model is compared with multiphase Navier-Stokes simulations in a parabolic fissure. Sampling the numerical results allows the isolation of flow factors such as surface tension, which are difficult to measure in physical experiments.

(72 pages)

PUBLIC ABSTRACT

Three Environmental Fluid Dynamics Papers

Eden Furtak-Cole

Three papers are presented, applying computational fluid dynamics methods to fluid flows in the geosciences. In the first paper, a numerical method is developed for single phase potential flow in the subsurface. For a class of monotonically advancing flows, the method provides a computational savings as compared to classical methods and can be applied to problems such as forced groundwater recharge. The second paper investigates the shear stress reducing action of an erosion control roughness array. Incompressible Navier-Stokes simulations are performed for multiple wind angles to understand the changing aerodynamics of individual and grouped roughness elements. In the third paper, a 1D analytical flow model is compared with multiphase Navier-Stokes simulations in a parabolic fissure. Sampling the numerical results allows the isolation of flow factors such as surface tension, which are difficult to measure in physical experiments.

ACKNOWLEDGMENTS

Thanks to all the people who told me to finish this, and the Utah Center for High Performance Computing for their technical help.

Eden Furtak-Cole

CONTENTS

LIST OF TABLES

LIST OF FIGURES

INTRODUCTION

Three papers are presented pertaining to environmental fluid dynamics. Modeling, simulation, numerical techniques, analytical methods, and physical experiments are all used to describe flows that occur naturally in the environment. Near surface phenomenon are a focal point, with pertinent flow examples drawn from micrometeorology and groundwater flow in the vadose zone or lower.

In the first paper, a numerical procedure is developed for a subsurface flow model. The model and solution procedure are directed at problems involving a variety of scales, where saturation fronts are sharp and advance monotonically. Forced groundwater recharge is an applicable problem, and is increasingly being employed under contemporary climate extremes. The method is also applicable to drawdown around wells or viscous flow in cracks. The proposed model can be applied in two or three spatial dimensions, and the procedure has the computational efficiency to be used at the landscape scale. This is achieved by limiting the implicit part of the solver to the saturated zone, and using a fast marching method to advance the saturation. Saturation fronts are tracked explicitly, and the method handles the merging of multiple fronts without issue. There are no stability limitations on the time step of the method, so a very limited number of implicit solves can be used if permitted by the physics of the problem.

In the second paper, flow over erosion control structures is investigated using the Navier-Stokes equations. Flow over a field experiment, deployed on the Owens Lake playa in California, is simulated for multiple wind angles. This field experiment was motivated by a massive dust problem, caused by the drying of Owens Lake due to a Los Angeles aqueduct diversion. Engineered roughness elements are considered as a last resort, where watering and vegetation plantings are not feasible. Such dust problems continue to emerge around the world. High wind shear drives the saltation of surface sediments, releasing small diameter particulate matter into the planetary boundary layer. Due to the large footprint and cost of engineered roughness elements, it is advantageous to maximize the efficiency of the

array configuration. Before this can be done, a basic understanding of their mechanism of shear reduction needs to be developed. Turbulent flow around the array is simulated for ten wind angles to study flow characteristics that can not be measured in the field experiment. Additional simulations illustrate flow characteristics around single elements.

The third paper investigates basic flow assumptions of a one dimensional nonlinear diffusion equation by comparing a similarity solution with numerical simulations of multiphase flow. This work is motivated by physical Hele-Shaw experiments of viscous gravity currents. Gravity currents occur when a density gradient exists between two fluids, resulting in gravity driven movement. These experiments model a variety of natural phenomenon, present in both the atmosphere and subsurface. For viscous spreading, we assume that these natural phenomenon operate at scales, velocities, and viscosities that allow turbulence to be neglected. In experiments, poor agreement with one dimensional models is often observed where the Dupuit-Forchheimer assumption is invalid. This assumption states that the one dimensional horizontal velocity can be calculated using the gradient of hydrostatic pressure and vertical averaging. It is difficult to separate the effects of three dimensional velocity from the influence of surface tension and capillary. Additionally, initial conditions in experiments can not be configured to match similarity solutions. Numerical simulations offer great flexibility in all flow conditions and parameters. This allows for the isolation of flow effects, including vertical velocity and surface tension.

A FAST MARCHING SOLUTION PROCEDURE FOR POTENTIAL FLOW IN THE

SUBSURFACE

A fast marching solution procedure for potential flow in the subsurface

Eden Furtak-Cole

Utah State University, Department of Mathematics and Statistics, Logan, UT 84322

Geordie Richards

Utah State University, Department of Mechanical and Aerospace Engineering, Logan, UT 84322

(Dated: December 6, 2017)

A numerical method is presented to solve flow problems in porous media and viscous spreading. A potential problem is implicitly solved, from which velocity is obtained. Saturation is advanced forward using a highly efficient fast marching method. This incremental procedure is applicable to wide variety of problems where the saturation front advances monotonically. The method presented is free of stability constraints, tracks the moving front explicitly, and can handle the merging or splitting of multiple fronts. The presented method is fast enough for applications on large computational domains with variable parameters.

I.   INTRODUCTION

Viscous gravity currents occur when the density difference between two fluids causes movement under the force of gravity or buoyancy. This takes place in a variety of natural and industrial settings. Avalanches[1] and pyrophastic flows[2] gain enormous momentum due to a density difference with air, and are miscible flows. Industrial CO_2 sequestration methods[34] pump brine of relatively low density under capped aquifers, where it spreads due to a buoyancy force. Groundwater flows provide important natural resources and are primarily driven by gravitational forces[56]. Many flows of interest, such as those involving air and water, can be modeled as immiscible. Due to orders of magnitude differences in density and viscosity, it is often reasonable to model these systems as single phase flows. Using lubrication theory, it is possible to convert between equivalent mathematical problems in porous media and laminar flow[6]. Thus, the same system of equations can be used to model porous media flow and the flooding of cracks in fractured media or a Hele-Shaw cell[7].

Many analytical approaches to single-phase immiscible flows have used the Dupuit-Forchimer (DF) assumption, resulting in the Boussinesq[8910] and Generalized Boussinesq[11121314] equations. These approaches assume horizontal-only velocity, and impose conservation on the height of the free surface[11]. Similarity variables can be used to solve a large class of these non-linear diffusion problems, in particular those with power-law boundaries and hydraulic conductivity. These typically involve initially saturated or initially dry conditions[131516]. This presents the problem that the early-time free surface is close to vertical, and will produce large vertical velocities. The fitness of the DF assumption to a particular problem exists on a continuum of free surface gradients, and it is not clear what effects the poorly represented physics of the early time solution will have on the later time results. This issue has motivated the use of experiments in conjunction with analytical methods. Lab-scale experiments often take the form of a Hele-Shaw cell, where fluid is passed between two plates in a lubercation theory setting. Hele-Shaw cells can be constructed from clear planar[1718] or curved[1920] plates, and are sometimes filled with porous media such as glass beads[1820].

Numerical approaches to multiphase flow in porous media have a long history of development[2122]. While these methods may be accurate, they require large amounts of computing power, and may not be necessary for problems where the gaseous phase can be safely disregarded. A similar model for one phase flow is the theory of potential flow[2320]. For problems that are not time steady, a numerical method is required to evolve the free surface. Level set methods[2425] are a relatively new method for tracking evolving interfaces, such as the free surface between fluid phases[262728].

In short, this method works by tracking the expected time of arrival of the front on a grid of points, rather than tracking points on the front itself. This results in a relaxation of the Courant-Friedrichs-Lewy (CFL) condition, sub-grid accuracy, and a natural handling of free surface merging or splitting. The fast marching method (FMM) is a special case of the level set methods, where the monotonicity of the front can be exploited for large computational savings. Few studies have applied level set methods to potential flow problems in groundwater dynamics. Garzon et al.[29] posed a number of potential flow problems using the level set method, and presented results for a breaking wave. Frolkovic[30] applied the level set method to groundwater flow, using a immersed interface method to extend the pressure outside the saturated zone.

We approach the problem of viscous spreading using a potential function to generate two-dimensional velocity, and a fast marching method to advance the saturation zone. This approach is applicable to monotonically advancing free surfaces, and can be used to model many problems in groundwater hydrology or Hele-Shaw experiments that involve sharp interfaces. The implicitly solved matrix problem for the potential is limited to the saturated zone, reducing the computation cost as compared to conventional methods. Because the DF assumption is never applied, the model retains full dimensional velocity. Moreover, the height-based potential function can easily be constructed with field measurements of an aquifer's phreatic surface for the generation of initial conditions.

The paper is organized as follows. A model of flow is given in section II, the numerical procedure in section III, numerical experiments are presented section IV, and the conclusions follow in section V.

II. FLOW MODEL

We consider the flow of a liquid displacing a gaseous phase in porous media. The liquid is considered incompressible and conservation of mass within the saturated zone dictates that the velocity is divergence-free:

$$\nabla \cdot \mathbf{u} = 0. \tag{1}$$

Velocity is given by Darcy's law,

$$\mathbf{u} = -\frac{k(\mathbf{x})}{\mu}(\nabla p + \rho g \mathbf{j}), \tag{2}$$

where the permeability of the media $k\left(\mathbf{x}\right)$ may be a function of space, μ is the viscosity, p is pressure, ρ is the fluid density, and g is gravity. At the free surface, we have the pressure boundary condition,

$$p = p_0 + (\rho - \Delta\rho)\, g\, (h_0 - h), \tag{3}$$

where $\Delta\rho$ is the density difference between the two phases, and h is height measured from some universal datum. For a system with a large density difference between the two phases, such as air and water, it can safely be assumed that $\rho = \Delta\rho$. We introduce the conserved quantity,

$$\varphi = \frac{p}{\rho g} + z, \tag{4}$$

which has units of height and can be interpreted as conservation of head in hydrology applications. Solving for p and substituting into eq. (2), we have

$$\mathbf{u} = -\frac{k\left(\mathbf{x}\right)}{\mu} \left(\nabla \rho g \left(\varphi - z\right) + \rho g \mathbf{j}\right), \tag{5}$$

$$= -\frac{k\left(\mathbf{x}\right)}{\mu} \nabla \rho g \varphi, \tag{6}$$

Substituting this quantity into the continuity equation eq. (1) gives a PDE for potential,

$$\nabla \cdot \left(k\left(\mathbf{x}\right) \nabla \varphi\right) = 0. \tag{7}$$

Substitution of eq. (4) into eq. (2) also gives a no flow boundary condition for horizontal impermeable surfaces,

$$\frac{\partial \varphi}{\partial z} = 0. \tag{8}$$

On the free surface, we assume that the effects of phase being displaced (i.e. air) are negligible, reducing the free surface boundary condition to,

$$p = p_0. \tag{9}$$

Substituting eq. (9) into eq. (4) gives,

$$\varphi = \frac{p_0}{\rho g} + z. \tag{10}$$

We observe that at the free surface, $z = h$ and p_0 can be taken as zero gauge pressure, resulting in

$$\varphi = h. \tag{11}$$

The above approach provides a potential equation and velocity calculations within the saturated zone. The liquid phase continuity equation is

$$\frac{\partial}{\partial t} \left(\phi \left(\mathbf{x} \right) \rho S \right) = -\nabla \left(\rho \mathbf{u} S \right) + q \quad S \in \{0, 1\}. \tag{12}$$

Here, q is a mass change due to sinks or sources. Saturation takes on discrete values of 1 for full saturation, and 0 for no saturation. The q term can be disregarded for fully saturated interfaces that are spatially distant from any sources or sinks. Incompressibility and time invariant porosity ϕ further simplifies the above to,

$$\phi \left(\mathbf{x} \right) \frac{\partial}{\partial t} \left(S \right) = -\mathbf{u} \cdot \nabla \left(S \right). \tag{13}$$

In 1-D eq. (13) reduces to the familiar problem of an advecting square wave that travels along characteristics, in 2-D the characteristics are streamlines from the potential flow function.

A. Special Cases of the Potential Equation

Important special cases of the potential equation eq. (7) are given by the form of the permeability function. The case of constant k results in the Laplacian potential equation,

$$\Delta \varphi = 0. \tag{14}$$

Using certain flow assumptions, this can be further reduced to the Boussinesq equation[20] and solved with a variety of methods[96,15,23]. Equation (14) can be solved numerically as an alternative to the Boussinesq equation when vertical motion is significant factor in in the problem of interest.

In the case of power-law permeability, $k \left(\mathbf{x} \right) = a z^n$. The resulting equation of potential flow is,

$$\frac{n}{z} \frac{\partial \varphi}{\partial z} + \Delta \varphi = 0. \tag{15}$$

This is analogous to the porous medium equation[133,11,416]. The spatial variability of the permeability is expressed as the addition of an advective term in the potential equation. The potential equation remains linear, while the associated porous medium equation is non-linear.

III. NUMERICAL PROCEDURE

We seek a numerical procedure to incrementally solve the system

$$\nabla \cdot (k(\mathbf{x}) \nabla \varphi) = 0, \tag{16a}$$

$$\mathbf{u} = -\frac{k\rho g}{\mu} \nabla \varphi, \tag{16b}$$

$$\phi(\mathbf{x}) \frac{\partial}{\partial t}(S) = -\mathbf{u} \cdot \nabla(S). \tag{16c}$$

The saturation equation is of particular interest, as we will be using the Fast Marching method to advance the saturated zone.

A. Fast Marching Methods and Stationary Formulation

The fast marching method is a well documented method for tracking monotonically advancing interfaces using the Eikonal equation[32][24]. The Eikonal equation is stated,

$$F\|\nabla T\| = 1, \tag{17}$$

where T is the arrival time, and F is a speed function. Equation (17) is solved in an an upwind manner to calculate the time T when the interface will arrive at various locations in the problem domain. The arrival times T provide a hypersurface, whose level sets in time are solution curves to the problem of interest. Monotonicity of the front dictates that information must move from places with smaller arrival times, to those with larger arrival times. The domain can be divided into three categories: points where the advancing interface has *arrived*, non-arrived points *near* the interface, and non-arrived points *far* from the interface. The narrow band method allows us to only operate on the *near* class of points to reduce computational cost.

Consider the interface ξ between the saturated and unsaturated zones in the solution of eq. (16c). The interface between the saturated and non-saturated zone denotes an evolving level set function of the form

$$\frac{\partial}{\partial t}(\xi) + \frac{\mathbf{u}}{\phi(\mathbf{x})} \cdot \nabla(\xi) = 0. \tag{18}$$

Then eq. (17) provides the arrival time T of the front ξ moving at speed $\frac{\mathbf{u}}{\phi(\mathbf{x})}$ for any point in the unsaturated part of the domain. Specifically, we seek a solution to the Eikonal equation where F has been replaced by the front speed,

$$\mathbf{u}\left(\mathbf{x}\right)\left\|\nabla T\right\| = \phi\left(\mathbf{x}\right). \tag{19}$$

Pseudo-code for the general FMM on a rectangular grid is given in algorithm 1. In addition to only having to operate on a small subset of the computational domain, the FMM gains efficiency from storing the narrow band in a min heap data structure. In this complete binary tree, the children of any node in the tree have larger arrival times than their parents. The smallest arrival time is always at the root of the tree, and computationally trivial to find. When a node is updated, moving up or down the tree takes at most $O(log(M))$ operations for an M sized narrow band[32].

Algorithm 1 Fast Marching Method (FMM)

1: Define *arrived*, *near* (narrow band), and *far* points
2: **while** size(*near*) > 0 **do**
3:      Let (i, j) be the index of the shortest arrival time T
4:      Tag surrounding *far* or *near* points $(\pm i, j)$ and $(i, \pm j)$ as neighbors. Reclassify the *far* as *near*
5:      Reclassify point (i, j) as *arrived* remove from *near*
6:      Update the arrival times T of all points tagged as neighbors.

A variety of methods are available for computing the new arrival times T. The simplest for a rectangular grid is the five point stencil[24]. Squaring both sides of eq. (19), we obtain

$$\left(\nabla T \cdot \mathbf{u}\left(\mathbf{x}\right)\right)^2 = \phi(\mathbf{x})^2. \tag{20}$$

Left and right derivatives are approximated by

$$D_x^{\pm} = \pm \frac{T_{i\pm 1,j} - T_{i,j}}{\Delta x}, \tag{21}$$

and

$$D_y^{\pm} = \pm \frac{T_{i,j\pm 1} - T_{i,j}}{\Delta y}. \tag{22}$$

Substituting these expressions into an upwind approximation of the term $\nabla T \cdot v(x)$ we have,

$$\left(\left(max(D_x^- T, 0) + min(D_x^+ T, 0)\right) + \left(max(D_y^- T, 0) + min(D_x^+ T, 0)\right)\right)^2 = 1. \tag{23}$$

Expansion of this expression yields a second order polynomial which can be solved by a variety of root finding methods.

B. Extending the Velocity

The fast marching method frees us from the limitations of the CFL condition. However, it is important to note that velocity is defined by eq. (16b) only inside the saturated zone. We use the method of[33] to extend the velocity using the fast marching method. This is accomplished by creating a signed distance function in the non-saturated part of the domain, and using a weighted average that is "upwind" with respect to distance to the front.

By solving the Eikonal equation for a constant front velocity of 1,

$$\|\nabla \eta\| = 1, \tag{24}$$

the resulting arrival times η are the distance from the front ξ. Initial values on ξ are defined by the initial data $\eta = T$ for the stationary problem. For the five point stencil eq. (23), distance is approximated linearly at the subgrid-scale.

To extend a variable outside the saturated zone, we seek a solution to the problem

$$\nabla \zeta_{ext} \cdot \nabla \eta = 0, \tag{25}$$

where η is the signed distance function, and ζ_{ext} is a scalar extended to the non-saturated zone. This constraint ensures the proper weighting of the spatial average, given the distance η. Since eq. (24) is solved with the fast marching method, the extension can be calculated explicitly at the same time as η. For the five point stencil in a 2D setting, two cases exist[33]. In the first case, η is calculated from one neighbor, and ζ_{ext} is simply a replication of the velocity in the neighboring cell. In the second case, η is calculated from two neighbors. Given η, eq. (25) can be solved for ζ_{ext} at the point (i, j) as

$$\zeta_{ext} = \frac{s^{-2}\zeta\left(i + s, j\right) + t^{-2}\zeta\left(i, j + t\right)}{s^{-2} + t^{-2}}, \tag{26}$$

where s and t are the distances to the neighboring cell centers in the x and y directions respectively and can take on negative values. This calculation is performed for each velocity component in place of ζ_{ext}. Alternatively, the scalar potential function can be extended and used for an explicit velocity calculation.

C. Time Stepping Procedure

We present the full solution algorithm in algorithm 2. We note two important aspects of controlling the solution accuracy and reducing floating point operations.

Algorithm 2 Solution procedure for the flow equations.

1: **for** $t_0..\Delta t..t_{end}$ **do**

2:     Solve eq. (16a) implicitly

3:     Calculate eq. (16b) explicitly

4:     Extend velocity using eq. (25)

5:     Advance eq. (16c) using algorithm 1

Extensions of the velocity do not overcome the problem of large time steps, as the true velocity changes dynamically with the free surface. The method is fast enough that for many applications it is possible to restrict the time step with CFL condition. This is the most conservative approach, and is dependent on mesh size. Alternatively, it is possible to restrict the time step to allow for an arbitrary distance of front travel before recalculating the potential. At any step in algorithm 2 the appropriate time step is simply

$$\Delta t = \frac{d_{max}}{u^\star_{max}}, \tag{27}$$

where d_{max} is the desired maximum travel distance for a given timestep, and $u^\star_{max}$ is the maximum velocity magnitude on the free surface.

The velocity calculation and extension need not be performed on the entire domain. In many applications, only resolving the movement of the free surface is required. If this is the case, velocity calculations only need to be performed on saturated cells adjacent to the free surface. Moreover, if the time step calculation eq. (27) is used, then the velocity extension can be terminated when the signed distance function eq. (24) reaches

$$\eta > d_{max}.$$

If a constant time step is used, velocity extension can be terminated when

$$\eta > \Delta t u^\star_{max}.$$

IV.   RESULTS

We present the results of a variety of simulation test cases, including a comparison to an analytical solution of the Boussinesq equation.

A.   Boussinesq-type Groundwater Infiltration

We compare the numerical procedure to a solution of the Boussinesq equation for a unsteady Dirichlet boundary condition. We choose the parameters shown in table I. This corresponds to the Boussinesq problem

$$\frac{\partial h}{\partial t} = \frac{k\rho g}{2\mu} \frac{\partial^2 h^2}{\partial x^2}, \tag{28}$$

with boundary condition,

$$h(0, t) = \sigma t^{1.5}; \tag{29}$$

for which a similarity solution exists[913].

TABLE I: Simulation parameters

Parameter	Value
permeability k	$10^{-6}\,\mathrm{m}^2$
density ρ	$1000\,\mathrm{kgm}^{-2}$
porosity ϕ	1
viscosity μ	$1\,\mathrm{Pa}\cdot\mathrm{s}$
scaling height σ	$0.01\,\mathrm{m}$

Results for the simulation and Boussinesq benchmark are shown in fig. 1. Excellent agreement is observed, with small differences profile shape. In particular, the two solutions show the greatest difference near the impermeable base. This is likely due to the vertical velocity modeled by the potential flow system. This system produces free surface profiles that are approximately twice the height of their width. Under these conditions, prominent vertical flow exists that is not modeled by the Boussinesq equation.
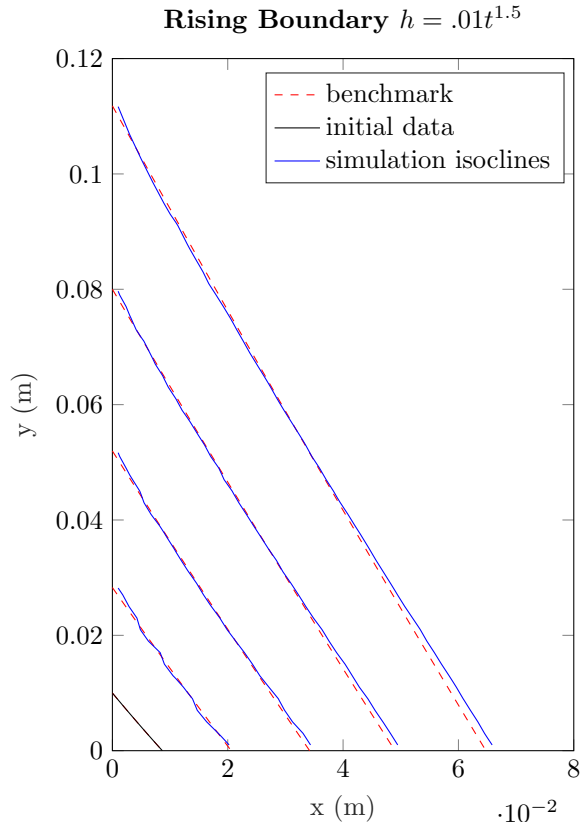
FIG. 1: A comparison of the Boussinesq and potential flow solutions at times $t = 1, 2, 3, 4, 5$. The initial data at $t = 1$ is given by an analytical solution to the Boussinesq equation. A Dirichlet boundary condition is applied to the left side, with saturation height rising as $h = .01t^1.5$.

B. Injection in a depleted aquifer

A slight modification of the potential function allows for the simulation of injection wells. We consider the case of a depleted aquifer with an impermeable bedrock base. Injection wells of various location and pressure are modeled as Dirac delta functions. The resulting potential equation is,

$$\Delta\varphi = \sum_i h'_i(t)\,\delta(x - x_i, y - y_i), \tag{30}$$

where h'_i is the potential given at the well. For gravity driven injection this is simply the height of water in the well, while injection with a specified pressure must be normalized by ρg.

fig. 2 shows the results of the injection problem with wells assigned potential values of 30 and 70 meters. Medium constants are given by table I, but dimension have been scaled to be realistic in hydrological applications. The merging of the two fronts is handled well by the fast marching method. To illustrate how the solution is embedded in a hypersurface, a surface plot of the arrival
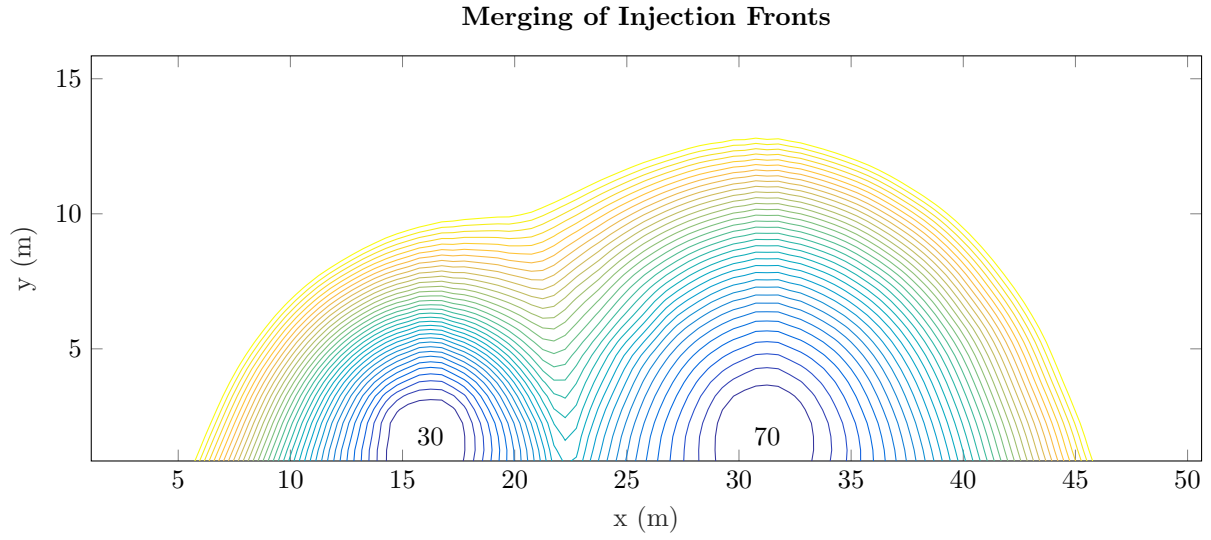
times is shown in fig. 3.

Merging of Injection Fronts

FIG. 2: Time isoclines for the solution of the injection problem. Values of the potential at the injection sites are shown.
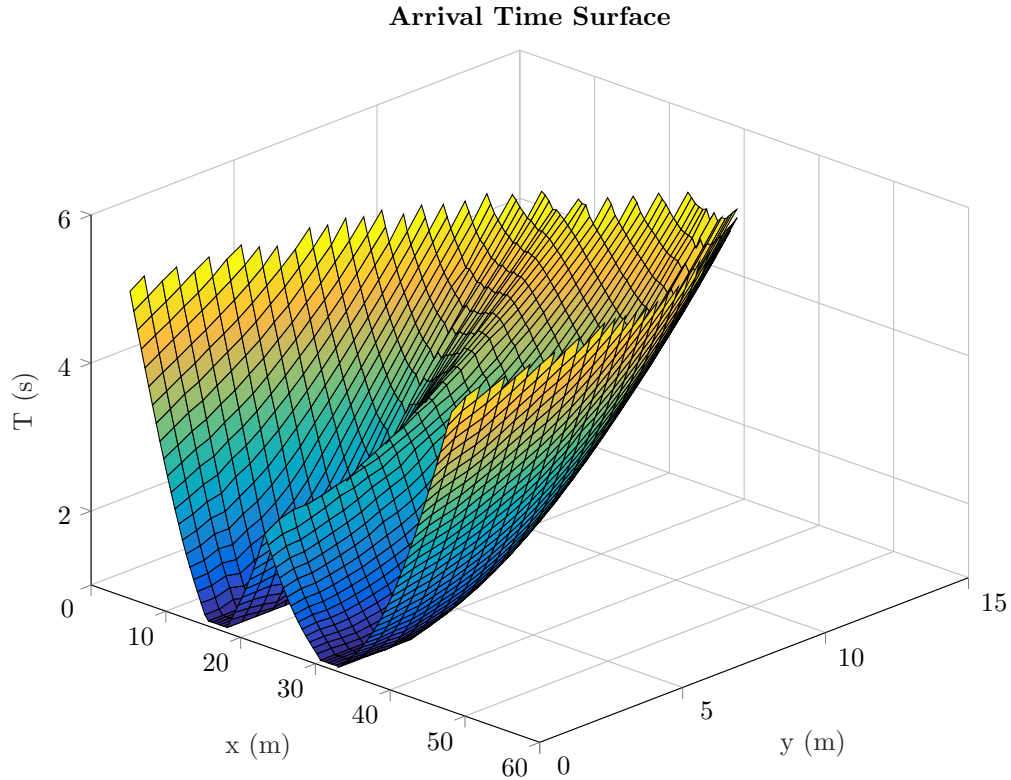
Arrival Time Surface

FIG. 3: Arrival times for the injection problem. Solution curves are level sets constructed by cutting at various locations on the z-axis. Areas around the injection wells are initially saturated at $t = 1$.

C. Flow over a tilted base

We now consider the case of a sloped aquifer or tilted Hele-Shaw cell. This is accomplished by modifying the gravity vector such that

$$\mathbf{g} = g\left(\sin\theta\mathbf{i} + \cos\theta\mathbf{j}\right), \tag{31}$$

where θ is the angle between the negative y-axis and the gravity vector. Then the Darcy velocity is

$$\mathbf{u} = -\frac{k\left(\mathbf{x}\right)}{\mu}\left(\nabla p + \rho g\left(\sin\theta\mathbf{i} + \cos\theta\mathbf{j}\right)\right). \tag{32}$$

While the mesh topology does not need to be changed, the potential needs to be measured in the direction of gravity. We define $z^\star$ as the z coordinate under the axis rotation θ, resulting in the

conserved quantity,

$$\varphi = \frac{p}{\rho g} + z^\star. \tag{33}$$

Then eq. (6) becomes,

$$\mathbf{u} = -\frac{k}{\mu}\left(\nabla \rho g \left(\varphi - z^\star\right) + \rho g \left(\sin\theta \mathbf{i} + \cos\theta \mathbf{j}\right)\right), \tag{34}$$

$$= -\frac{k}{\mu}\left(\nabla \rho g \varphi - \rho g \left(\sin\theta \mathbf{i} + \cos\theta \mathbf{j}\right) + \rho g \left(\sin\theta \mathbf{i} + \cos\theta \mathbf{j}\right)\right), \tag{35}$$

$$= -\frac{k}{\mu}\nabla \rho g \varphi, \tag{36}$$

and the resulting potential equation,

$$\Delta\varphi = 0. \tag{37}$$

This is conveniently the same result as eq. (14), with a modification to the boundary conditions. Potential on the free surface $h^\star$ is now measured in the direction of the gravity vector:

$$h^\star = \frac{z}{\cos\theta}, \tag{38}$$

Where z is measured above some universal datum.

We present results of a simulation modeled after experiments performed in[17]. Fluid is injected between two parallel plates using a potential of .23 meters. The parameters used in table I were reused with a $50°$ rotation of the gravity vector to produce the result shown in fig. 4. This simulation was performed on the same Cartesian mesh as used in fig. 2, with the coordinates projected to their true locations after the solution was produced. Time isoclines of the solution are elongated along the tilted base. Flow stagnates in the region between the injection and impermeable base.
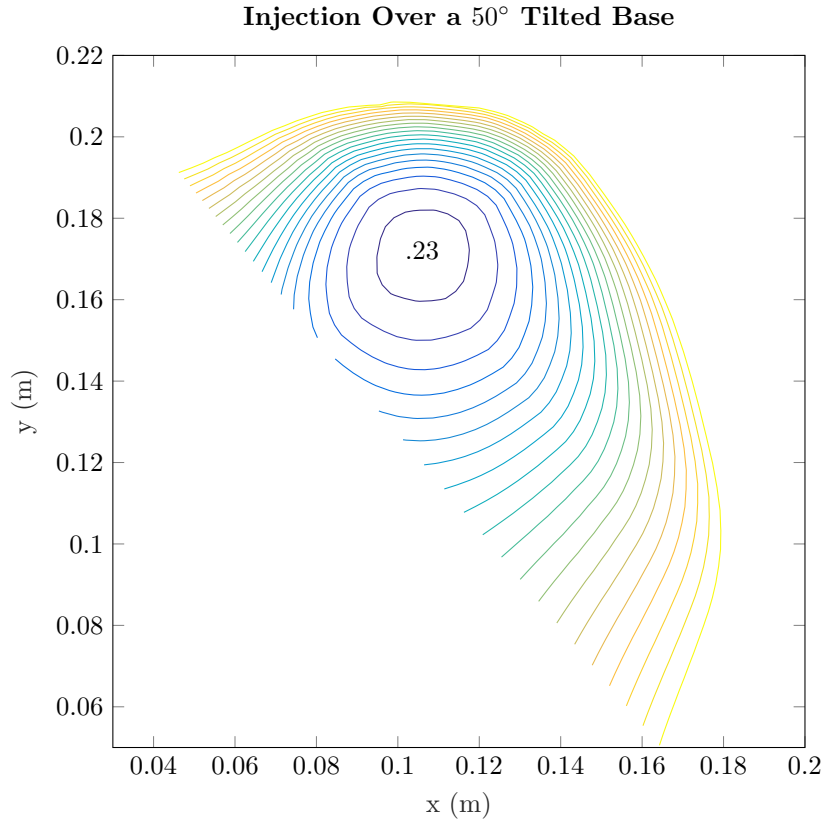
Injection Over a $50°$ Tilted Base

FIG. 4: Saturation curves in time for injection over a tilted surface.

V.   CONCLUSIONS

A numerical method was developed to solve potential flow problems in the subsurface. The method is limited to monotonically advancing flows, but is extremely fast. In a comparison with the Boussinesq equation, the method is shown to include the effects of vertical velocity, but maintains a similar rate of front propagation. The method is easily extended to problems where the potential is given by solving the Poisson equation, and remains stable under changing saturation front topologies. The method was also applied to a tilted aquifer problem by changing the gravity vector and re-calculating the boundary conditions.

[1]   Herbert Huppert. Gravity currents: A personal perspective. *Journal of Fluid Mechanics*, 554:299 – 322, 05 2006.

[2]   J E Simpson. Gravity currents in the laboratory, atmosphere, and ocean. *Annual Review of Fluid Mechanics*, 14:213–234, 11 1982.

[3] Marc Hesse, Hamdi Tchelepi, B J. CANTWEL, and F M. ORR Jr. Gravity currents in horizontal porous layers: Transition from early to late self-similarity. *Journal of Fluid Mechanics*, 577:363 – 383, 04 2007.

[4] M.J. Leahy, J. Ennis-King, J. Hammond, H.E. Huppert, and J. Neufeld. Application of gravity currents to the migration of co2 in heterogeneous saline formations. *Energy Procedia*, 1(1):3331 – 3338, 2009. ISSN 1876-6102. doi:https://doi.org/10.1016/j.egypro.2009.02.120. URL `http://www.sciencedirect.com/science/article/pii/S1876610209007632`. Greenhouse Gas Control Technologies 9.

[5] David B McWhorter and Daniel K. Sunada. *Ground-Water Hydrology and Hydraulics*. Water Resources Publications, 1977.

[6] Jacob Bear. *Dynamics of Fluids in Porous Media*. Dover Publications, 1988.

[7] Zhong Zheng, Beatrice Soh, Herbert E. Huppert, and Howard A. Stone. Fluid drainage from the edge of a porous reservoir. *Journal of Fluid Mechanics*, 718:558568, 2013. doi:10.1017/jfm.2012.630.

[8] D.A Lockington, J.-Y Parlange, M.B Parlange, and J Selker. Similarity solution of the Boussinesq equation. *Advances in Water Resources*, 23(7):725 – 729, 2000. ISSN 0309-1708. doi: http://dx.doi.org/10.1016/S0309-1708(00)00004-X. URL `http://www.sciencedirect.com/science/article/pii/S030917080000004X`.

[9] Zhi-yao Song, Ling Li, and Lockington David. Note on Barenblatt power series solution to Boussinesq equation. *Applied Mathematics and Mechanics*, 28(6):823–828, Jun 2007. ISSN 1573-2754. doi: 10.1007/s10483-007-0612-x. URL `http://dx.doi.org/10.1007/s10483-007-0612-x`.

[10] Panagiotis K. Tolikas, Epaminondas G. Sidiropoulos, and Christos D. Tzimopoulos. A simple analytical solution for the Boussinesq one-dimensional groundwater flow equation. *Water Resources Research*, 20 (1):24–28, 1984. ISSN 1944-7973. doi:10.1029/WR020i001p00024. URL `http://dx.doi.org/10.1029/WR020i001p00024`.

[11] Juan Luis Vazquez. *The Porous Medium Equation, Mathematical Theory*. Oxford University Press, 2007.

[12] G I. Barenblatt. *Scaling*. Cambridge University Press, 2003.

[13] G I. Barenblatt. On some unsteady-state movements of liquid and gas in porous medium. *Prikl. Mat. i Mekh.*, 16(1):67–78, 1952.

[14] Jeffrey S. Olsen and Aleksey S. Telyakovskiy. Polynomial approximate solutions of a generalized Boussinesq equation. *Water Resources Research*, 49(5):3049–3053, 2013. ISSN 1944-7973. doi: 10.1002/wrcr.20242. URL `http://dx.doi.org/10.1002/wrcr.20242`.

[15] Aleksey S. Telyakovskiy, Gasto A. Braga, Satoko Kurita, and Jeff Mortensen. On a power series solution to the Boussinesq equation. *Advances in Water Resources*, 33(9):1128 – 1129, 2010. ISSN 0309-1708. doi:http://dx.doi.org/10.1016/j.advwatres.2010.06.017. URL `http://www.sciencedirect.com/science/article/pii/S0309170810001296`.

[16] David E. Rupp and John S. Selker. Drainage of a horizontal Boussinesq aquifer with a power law hydraulic conductivity profile. *Water Resources Research*, 41(11), 2005. ISSN 1944-7973. doi: 10.1029/2005WR004241.

[17] Valentina Ciriello, Sandro Longo, Luca Chiapponi, and Vittorio Di Federico. Porous gravity currents: A survey to determine the joint influence of fluid rheology and variations of medium properties. *Advances in Water Resources*, 92:105 – 115, 2016. ISSN 0309-1708. doi: http://dx.doi.org/10.1016/j.advwatres.2016.03.021. URL `http://www.sciencedirect.com/science/article/pii/S0309170816300835`.

[18] V. Di Federico, S. Longo, Stuart King, L. Chiapponi, D. Petrolo, and V. Ciriello. Gravity-driven flow of herschel–bulkley fluid in a fracture and in a 2d porous medium. *Journal of Fluid Mechanics*, 821:59–84, 6 2017. ISSN 0022-1120. doi:10.1017/jfm.2017.234.

[19] Zhong Zheng, Ivan Christov, and Howard A. Stone. Influence of heterogeneity on second-kind self-similar solutions for viscous gravity currents. 747, 04 2014.

[20] Sandro Longo, Valentina Ciriello, Luca Chiapponi, and Vittorio Di Federico. Combined effect of rheology and confining boundaries on spreading of gravity currents in porous media. *Advances in Water Resources*, 79:140 – 152, 2015. ISSN 0309-1708. doi:http://dx.doi.org/10.1016/j.advwatres.2015.02.016. URL `http://www.sciencedirect.com/science/article/pii/S0309170815000482`.

[21] Donald W. Peaceman. *Fundamentals of Numerical Reservoir Simulation*. Elsevier, 1977.

[22] Rainer Helmig. *Multiphase Flow and Transport Processes in the Subsurface*. Springer, 1997.

[23] P.Y. Polubarinova-Kochina. *Theory of Groundwater Movement*. Princeton University Press, 1962.

[24] J. A. Sethian. *Level Set Methods and Fast Marching Methods*. Cambridge University Press, 1996.

[25] J. A. Sethian. Computational methods for advancing interfaces. *World Scientific*, 2001.

[26] Mark Sussman, Peter Smereka, and Stanley Osher. A level set approach for computing solutions to incompressible two-phase flow. *J. Comput. Phys.*, 114(1):146–159, September 1994. ISSN 0021-9991. doi:10.1006/jcph.1994.1155. URL `http://dx.doi.org/10.1006/jcph.1994.1155`.

[27] Y.C. Chang, T.Y. Hou, B. Merriman, and S. Osher. A level set formulation of eulerian interface capturing methods for incompressible fluid flows. *Journal of Computational Physics*, 124(2):449 – 464, 1996. ISSN 0021-9991. doi:http://dx.doi.org/10.1006/jcph.1996.0072. URL `http://www.sciencedirect.com/science/article/pii/S0021999196900728`.

[28] J. A. Sethian and Peter Smereka. Level set methods for fluid interfaces. *Annual Review of Fluid Mechanics*, 35(1):341–372, 2003. doi:10.1146/annurev.fluid.35.101101.161105. URL `https://doi.org/10.1146/annurev.fluid.35.101101.161105`.

[29] M. Garzon, N. Bobillo-Ares, and J.A. Sethian. Some free boundary problems in potential flow regime using a based level set method. *Nova*, Dec 2008. URL `http://www.osti.gov/scitech/servlets/purl/948033`.

[30] P. Frolkovic. Application of level set method for groundwater flow with moving boundary. *Advances in Water Resources*, 47:56 – 66, 2012. ISSN 0309-1708. doi: http://dx.doi.org/10.1016/j.advwatres.2012.06.013. URL `http://www.sciencedirect.com/science/article/pii/S0309170812001777`.

[31] G I. Barenblatt. On some problems of unsteady filtration (in russian). *Izv. AN SSSR*, (6):97–110, 1954.

[32] J. A. Sethian. A fast marching level set method for monotonically advancing fronts. *Proceedings of the National Academy of Sciences*, 1995.

[33] D. Adalsteinsson and J. A. Sethian. The fast construction of extension velocities in level set methods. *Journal of Computational Physics*, 148(1):2–22, 1 1999. ISSN 0021-9991.

THE INFLUENCE OF WIND DIRECTION ON SHELTERING EFFECTS OF

EROSION CONTROL ROUGHNESS ARRAYS

The influence of wind direction on sheltering effects of erosion control roughness arrays

Eden Furtak-Cole

Utah State Univeristy, Department of Mathematics and Statistics, Logan, UT 84321

John A. Gillies

Desert Research Institute, Division of Atmospheric Science, Reno, NV 89503

(Dated: December 6, 2017)

We combine field and computational fluid dynamics (CFD) approaches to investigate the ability of roughness elements to control sand flux and dust emissions. Few experiments have examined the combined influences of wind angle and array configuration on shear stress reduction on the ground surface between elements. We show that a CFD approach can reproduce the average roughness array in a field setting. Computational results corroborate field observations of a dramatic reduction in velocity over the first two rows of roughness elements. We report the time averaged shear as a function of wind angle for single elements and the experimental array. Results show effective shear reduction through a wide range of wind angles. The array is shown to perform well at wind angles close to diagonal corridors and poorly for wind angles close to corridors running through the element rows. Simulations around single elements show that complicated aerodynamics play a dominant role over single parameter estimates of shear reduction.

I.   INTRODUCTION

Wind erosion is a problem around the world, with small particulate matter being of particular health concern to humans and livestock[1234]. Areas with high winds and changing land surfaces are of particularly problematic. Roughness arrays composed of simple bluff bodies offer a flexible and affordable way to control saltation and entertainment of particulate matter into the planetary boundary layer[5]. An example of a controlled surface is the Owens lake playa, where the diversion of water for anthropogenic uses has exposed fine lake bed sediments to high winds and various control measures have been placed to reduce sand transport and the accompanying dust emmisions[67].

Roughness elements have been most studied in the context of their effects on air flow in the urban canopy. Scaled models have been studied in wind tunnels[891011] and have included the effects of live vegetation on affecting boundary shear stress[12]. To deal with the limitations of boundary conditions and the sparsity of velocity measurements, computational fluid dynamics (CFD) simulations have been validated against wind tunnel results. Less work has been done for the direction modeling of field measurements. This has been performed for various configurations of single or multiple cubes, and to validate the applicability of $k - \epsilon$ Reynolds averaged Navier-Stokes (RANS)[1314], large eddy simulation (LES)[14151617], and DNS[189] methods. In a comparison of LES and $k - \epsilon$ turbulence closeures, Cheng et al.[14] found the $k - \epsilon$ model to be sufficient in modeling large scale motions, such as those that would cause sediment transport. Martilli and Santiago[19] investigated the vertical motions around roughness elements using the $k - \epsilon$ turbulence model in the context of the urban canyon after experimental validation by Santiago et al.[13]. We are unaware of any numerical studies have been directed at the use of roughness elements for erosion control or their changing effectiveness under a rotated velocity field.

Field studies have validated the success of roughness arrays in controlling wind erosion[4]. However, measured saltation is time integrated over a variety of atmospheric conditions. Gillies et al.[5] conducted a field study using straw bales to stabilize the Keeler dune system in the Owens Valley, CA. Irregular placement of elements was demonstrated to effectively remove saltating particles from the atmosphere, meeting target sand reductions. A Gillies et al.[20] experimentally investigated shear stress within staggered cylinder arrays in the atmospheric surface layer, finding a strong relationship between roughness density and shear reduction. Abulaiti et al.[21] conducted similar field experiments to assess the effectiveness of plants to stabilize coastal sand dunes from wind erosion as a function of their frontal area.

While roughness arrays have been successfully deployed to reduce wind erosion, their mechanism

of action is not fully understood. Flow fields are difficult to measure in physical experiments without disruption and most measurement methods result in sparse data. It is difficult to replicate turbulent atmospheric boundary conditions in both wind tunnels and Computational Fluid Dynamics (CFD) simulations. A common approach to predicting the boundary layer resulting from the addition of roughness elements is to base a roughness parameter on the total frontal area of the array[22][23]. While this estimate can be effective in matching field measurements, it neglects the spatial distribution of the elements and their aerodynamic properties. To fully understand why arrays of roughness elements successfully reduce the saltation of ground level sediments, it is necessary to view the flow field around the individual elements.

In this paper, we take a CFD approach to understanding the shear reducing action of a roughness array. The finite volume method toolbox openFOAM[24][25] is employed to solve the Navier-Stokes equations (NSE) over a replicated section of a field experiment deployed on the Owens Lake playa in California (Gillies et al., submitted). Additional single element simulations are conducted as a baseline to differentiate the influence of interacting shelter zones verses the sheltering of a single element. We investigate the effectiveness of the array to decrease surface shear stress in the lee-side shelter zone under different wind approach angles. Our approach accounts for the changing aerodynamics of individual elements. Moreover, we quantify the distribution of shear stress reduction experienced by the ground surface.

II.   FIELD EXPERIMENT

Engineered roughness elements (ERE) were deployed on the crusted playa surface of Owens Lake, CA, where sand transport was known to occur. Elements were commercially available plastic bins, with a footprint of $0.725\,\text{m} \times 0.45\,\text{m}$ and a vertical height of $0.38\,\text{m}$. Elements were arranged in staggered rows, with a $2.48\,\text{m}$ spacing between elements, as shown in fig. 1. The total array size measured $100\,\text{m} \times 100\,\text{m}$. The array was positioned so that the staggered rows are oriented transverse to the prevailing wind direction.

Three $10\,\text{m}$ towers were erected at locations upwind of the array, at the array edge, and $50\,\text{m}$ into the array. From anemometer measurements collected on the towers external to the array, we estimate the roughness of the crusted playa at $0.05\,\text{m}$. Cup anemometers were placed at 20 locations within the array at a height of $0.25\,\text{m}$ ($0.58\,\text{element height}$). Locations were chosen in relation to repeating patterns within the staggered rows, as shown in fig. 2. The pattern presented in fig. 2 is repeated four times downwind into the array. In addition to cup anemometers, four wind vanes

FIG. 1: ERE deployed at the Owens lake site.

were placed in the array between $1.24\,\mathrm{m}$ (ND=3.26) and $43.4\,\mathrm{m}$ (ND=114.21) with anemometers at positions 1 and 4 (fig. 2), respectively, at $50.8\,\mathrm{m}$ (ND=133.79) and $2.1\,\mathrm{m}$ (ND=137.05).
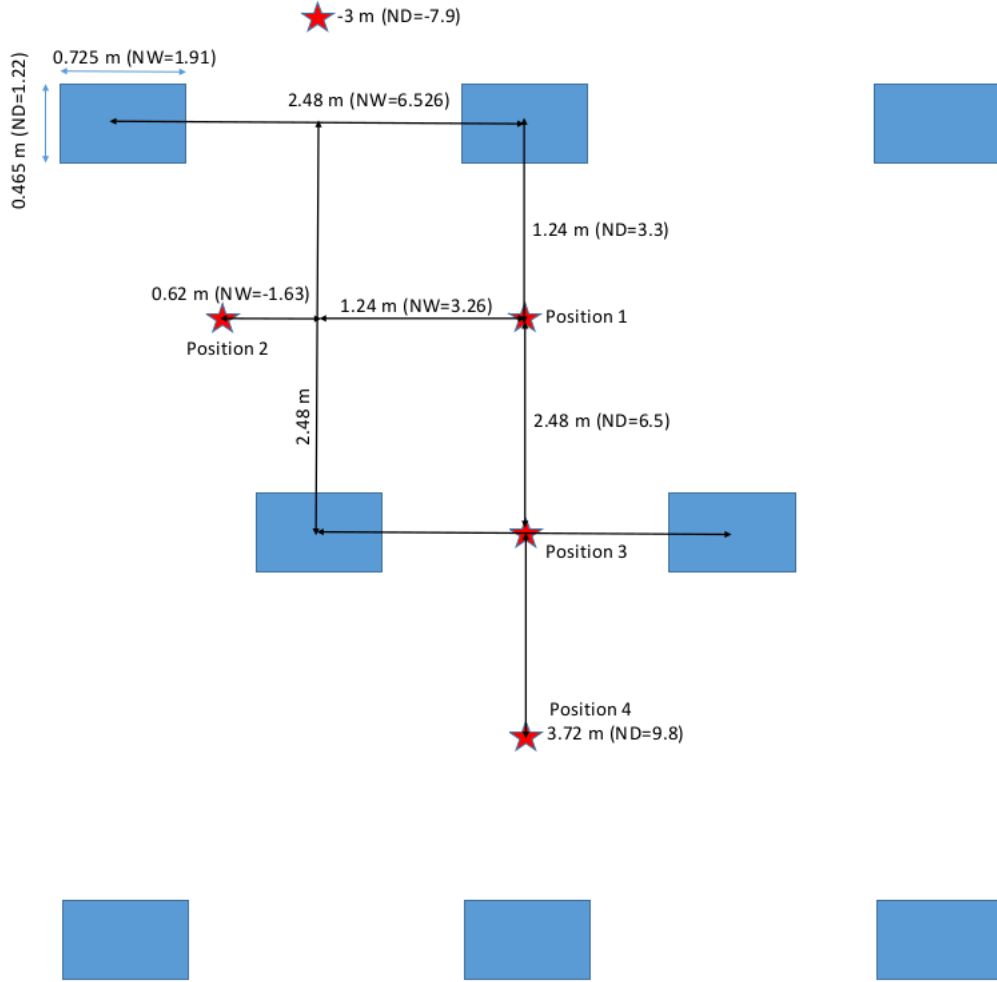
FIG. 2: Spacing and location of the anemometers relative to the roughness elements. Normalized distance (ND=horizontal distance/element height) and normalized width (NW=lateral distance/element height) are reported. Four wind vanes were placed at position 4.

III.   GOVERNING EQUATIONS AND BOUNDARY CONDITIONS

We seek numerical solutions to the incompressible Navier-Stokes Equations (NSE) over a 30 m wide section (NW=78.95) of the ERE experiment extending 50 m downwind into the array. The computational domain extends from the ground to a height of 10 m to match the height of the regional towers. The incompressible NSE are stated,

$$\rho \frac{D\mathbf{u}}{Dt} = -\nabla p + \rho \mathbf{g} + \mu \Delta \mathbf{u}, \tag{1}$$

$$\nabla \cdot \mathbf{u} = 0, \tag{2}$$

and represent conservation of momentum and mass, respectively. Here, ρ is fluid density, p pressure, $\mathbf{u}$ velocity, and $\mathbf{g}$ is a gravity vector. Due to the large computational domain and need to resolve flow between roughness elements, a $k - \epsilon$ turbulence model was employed. All simulations were performed using the finite volume solver openFOAM[24][25]. The time dependent NSE were solved using the semi-implicit method for pressure linked equations (SIMPLE) solver, simpleFoam.

Boundary conditions were implemented following Hargreaves and Wright[26], based on the atmospheric log layer presented by Richards and Hoxey[27]. At the inlet, the equations for horizontal velocity u, turbulent kinetic k, and dissipation rate ϵ are

$$u = \frac{u_\star}{\kappa} \ln \left(\frac{z + z_0}{z_0} \right), \tag{3}$$

$$k = \frac{u_\star^2}{\sqrt{C_\mu}}, \tag{4}$$

$$\epsilon = \frac{u_\star^3}{\kappa \left(z + z_0 \right)}, \tag{5}$$

where $u_\star$ is the friction velocity, z_0 the surface aerodynamic roughness length, κ von Karman's constant, and C_μ is an empirically determined constant from the $k - \epsilon$ turbulence model. The above quantities were assigned to be zero gradient with respect to the outward normal vector of the outlet patches.

Standard wall functions were used on the smooth surface of the roughness elements. The ground surface was assigned a rough turbulent viscosity wall function to reflect the measured roughness length of $0.05\,\mathrm{m}$. The upper atmosphere boundary was assigned a horizontal velocity of $15\,\mathrm{ms}^{-1}$ to represent a geostrophically driven planetary boundary layer[26]. This value represents a common wind speed at a $10\,\mathrm{m}$ height which reliably produces saltation on the ground.

IV.   COMPUTATIONAL EXPERIMENTS

We perform a series of computational experiments in two settings. In both cases, we simulate an atmospheric boundary layer over a height of $10\,\mathrm{m}$. In the first, we replicate the field experiment described in section II. After mesh generation, simulations were run for wind angles from $0°$ to $90°$ at $10°$ increments. Sampling of the velocity and surface shear were conducted on a grid oriented parallel to the flow direction. Surface shear was sampled directly from the stress tensor.

The second computational experiment was designed to isolate the effects of a single roughness element, as opposed to the interacting effects in the first experiment. In this experiment, nine meshes were produced by rotating the single element geometry to the same wind angles as the
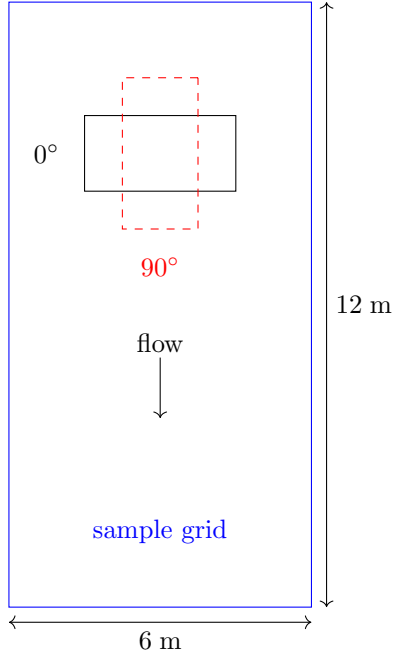
FIG. 3: A birds-eye schematic of the computational experiment and and sampling area.

array experiment. In this case, the sampling grid was re-used on each of the meshes. A schematic of this experiment is presented in fig. 3.

The muli-element mesh produced contained approximately 5×10^8 finite volume cells. A hexahedral $1\,\mathrm{m}$ base mesh was used, with four progressive refinement levels performed as a function of height. All surfaces were refined to 6 levels, with three cell refinements for each level. For the computational experiment depicted in fig. 3, the number of cells in each mesh are on the order of 10^7. Each mesh was generated from a $0.5\,\mathrm{m}$ hexahedral base mesh. Two subdivisions were performed for each refinement level. Each surface was refined to a minimum of 6 levels, with additional refinement levels of 5 and 2 performed for all cells within $1\,\mathrm{m}$ and $2\,\mathrm{m}$ of the ground, respectively.

V. RESULTS

A. Validation of Simulations With Field Data

Results for the zero degree wind angle simulation are validated against field data. A comparison between the single velocity simulation and unsteady field conditions is made possible by normalizing the interior velocity measurements with a velocity measurement outside of the array, defined as the wind speed ratio WSR. Comparisons of measured vs. modeled WSR are given in fig. 4 for position 1 and 3. In both positions, the simulation results show a lower reduction in wind speed ratio. Field
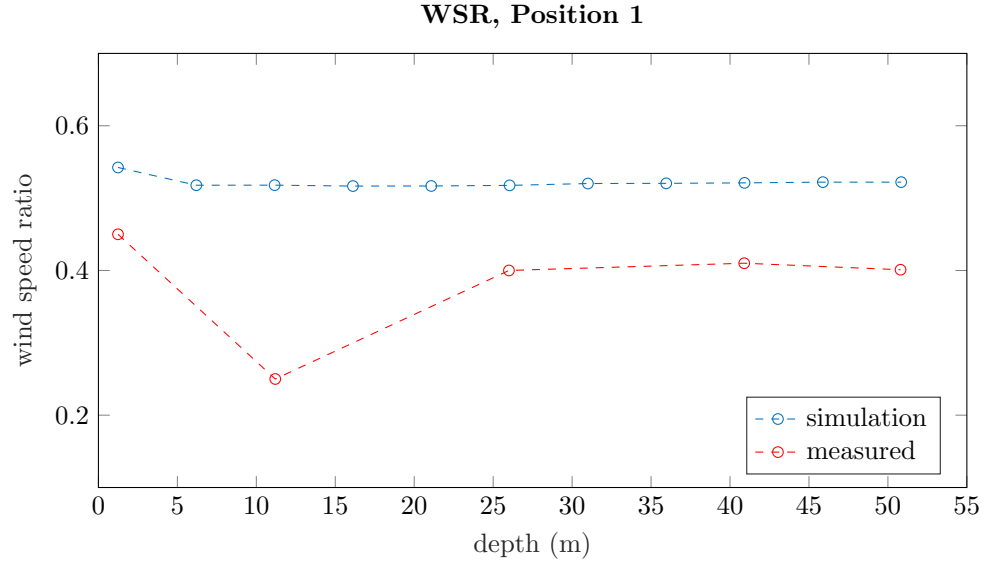
WSR, Position 1

(a) WSR comparison for position 1 (ND=9.97).
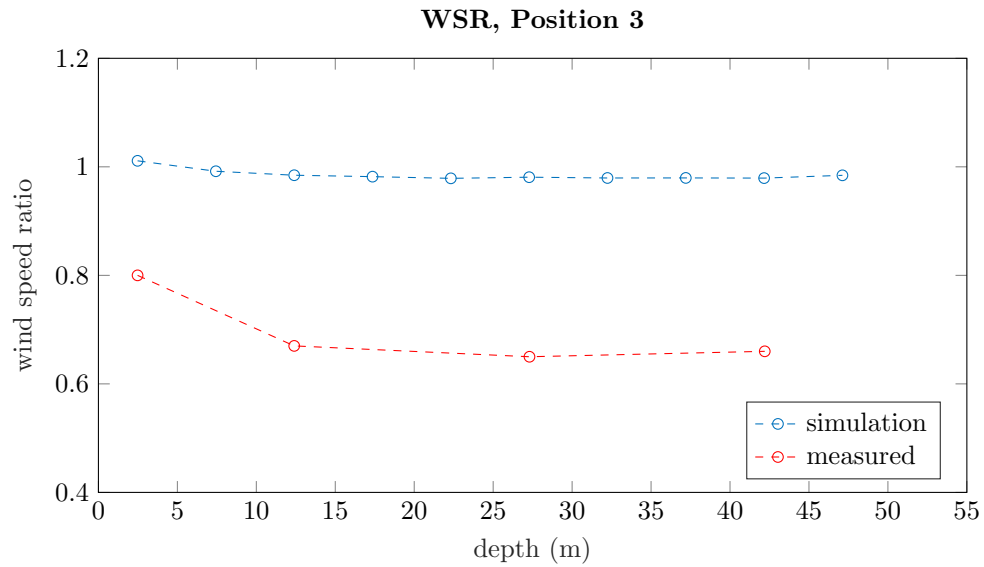
WSR, Position 3

(b) WSR comparison for position 3 (ND=75.05).

FIG. 4: WSR for positions 1 and 3.

measurements were taken using cup anemometers, which only measure velocity in the horizontal plane. It is likely that flow separation behind the elements caused misreadings where strong vertical flow components are neglected in the field data. By contrast, simulated wind speed was calculated with a vector Euclidean norm, which accounts for all directions of flow. Additionally, the field data are one minute averages of a highly unsteady wind field, which contains measurements from a wind direction range spanning $20°$.

Shear Magnitude for Ten Wind Angles
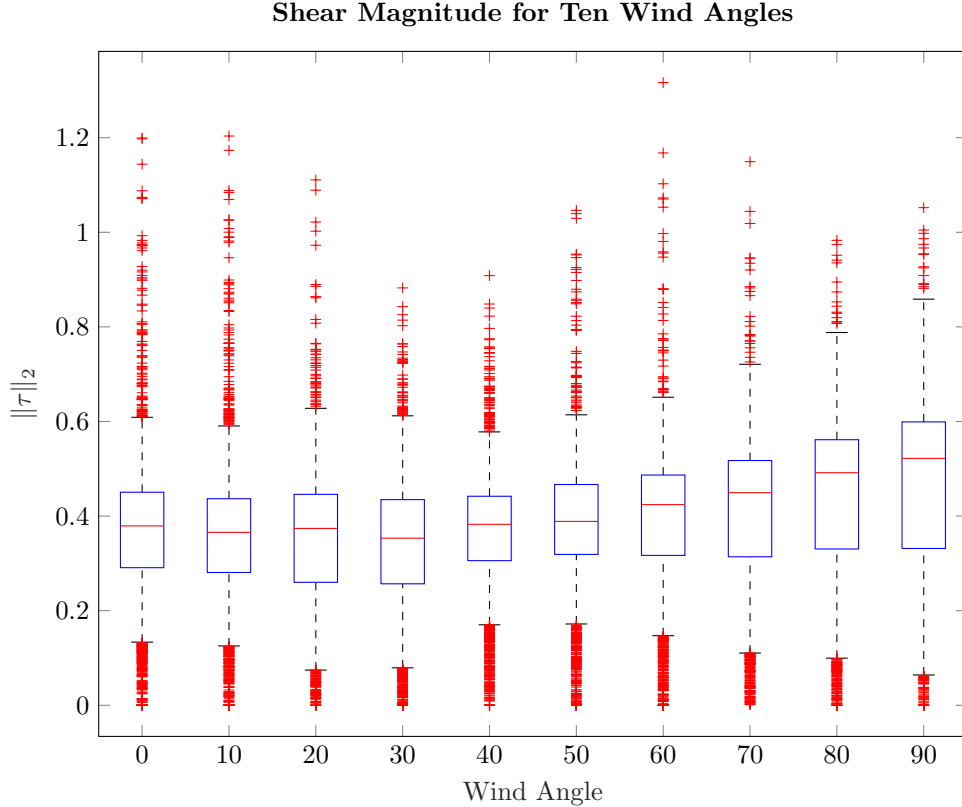
FIG. 5: A boxplot of shear values, sampled $14\,\mathrm{m}$ to $30\,\mathrm{m}$ into the array. Whisker lengths represent one interquartile range.

B.   Shear Stress Reduction and Wind Angle

Field and numerical observations indicate that for all wind angles, wind speed reduction mostly occurs within two to three rows of roughness elements. Shear was temporally averaged for the last 40 seconds of simulation to understand the effects of wind direction. We then sampled the area from $14\,\mathrm{m}$ to $30\,\mathrm{m}$ meters into the array. This region is conservatively beyond the initial wind profile adjustment zone and sufficiently far from the numerical influence of any outlet boundaries. Boxplots of this sampling are shown in fig. 5. The array remains highly effective in reducing shear for angles ranging from $0°$ to $50°$. Average shear increases as the wind angle approaches $90°$. At this angle, wind travels between the rows without encountering obstacles, and elements are aerodynamically aligned with their short edges facing the wind direction.

Wind angles $20°$ and $30°$ are particularly interesting, as diagonal corridors occur through the array at an angle of approximately $26.5°$. Corridors have a width of approximately $2.77\,\mathrm{m}$, as measured from the element centers. The angles of $20°$ and $30°$ have higher shear stress variability
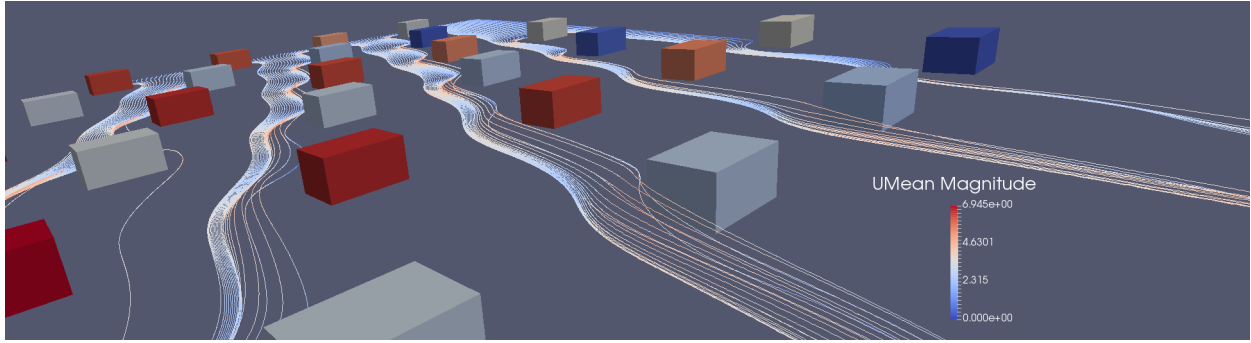
(a) Streamlines through the Mean velocity field, seeded upwind of the roughness array at a height of 0.1 m.
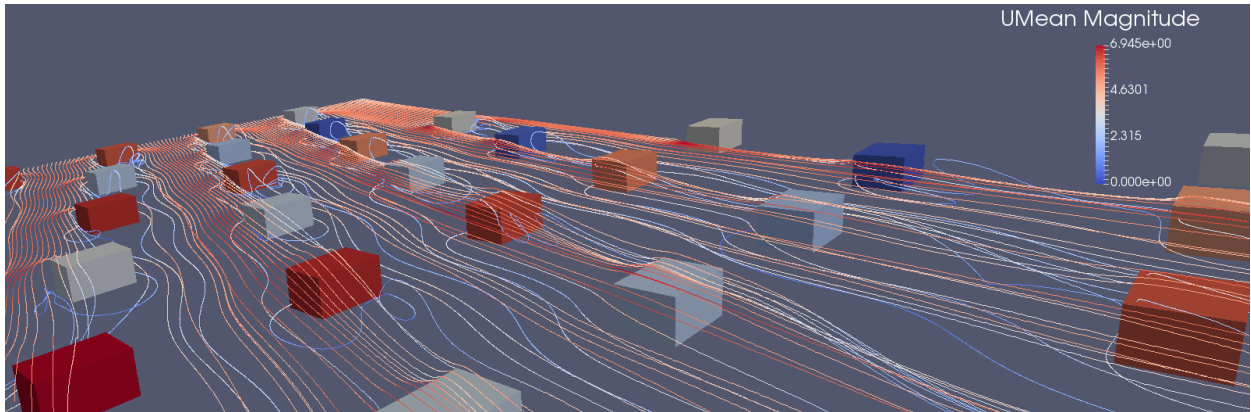

(b) Streamlines through the Mean velocity field, seeded upwind of the roughness array at a height of 0.2 m.

FIG. 6: 6a) Near ground streamlines are channeled, and eventually collide with roughness elements. 6b) Mid-level streamlines loose velocity in the turbulent wakes of the roughness elements, and are eventually channeled over the tops of roughness elements. In both figures streamlines are colored to represent magnitude of mean velocity, blue being slow and increasing speed represented with deepening red color. Elements are arbitrarily colored by their ordering.

than the adjacent angles, but the median shear magnitude remains low. Streamlines through the time-averaged flow field in fig. 6 illustrate the cause of this phenomenon. As streamlines released at 0.1 m come into contact with the first row of elements (fig. 6a), they are compressed horizontally into channels, which are later driven over elements deeper in the array. By this mechanism shear reduction is created around the roughness elements, perpendicular to the wind direction. Streamlines released at a height of 0.2 m, shown in fig. 6b, interact with the horseshoe vorticies and wake that form around the elements. This results in a loss of velocity magnitude. Streamlines that do not interact with the turbulence around the elements are weakly channeled, and eventually driven over elements as they travel through the array.

Spatial averaging was performed on the temporally averaged data in the direction perpendicular

to the inlet wind direction. Shear magnitude plotted as a function of depth into the array is shown in fig. 7 for three wind angles. These three plots underscore three important aspects of array design. In fig. 7a, the wind approaches at the angle the array was designed for. This results in a rapid reduction of the shear, but large oscillations result as the successive rows of roughness elements are encountered. This signal is largely dampened in the $30°$ simulation, as wind travels nearly parallel to the diagonal corridors. At $70°$, the flow begins to align with the element rows and the elements approach a their most aerodynamic alignment. Overall shear becomes higher as elements shelter each other, rather than the ground surface.

Average Shear, 0°
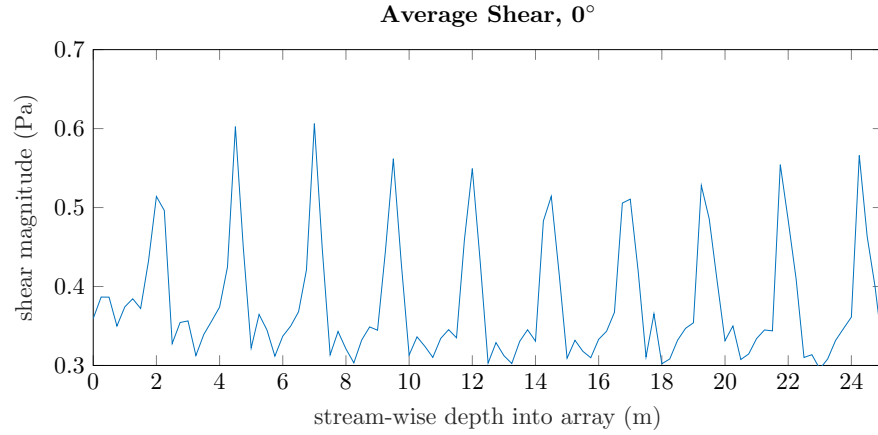
(a) Wind periodically encounters spanwise element rows head-on.

Average Shear, 30°
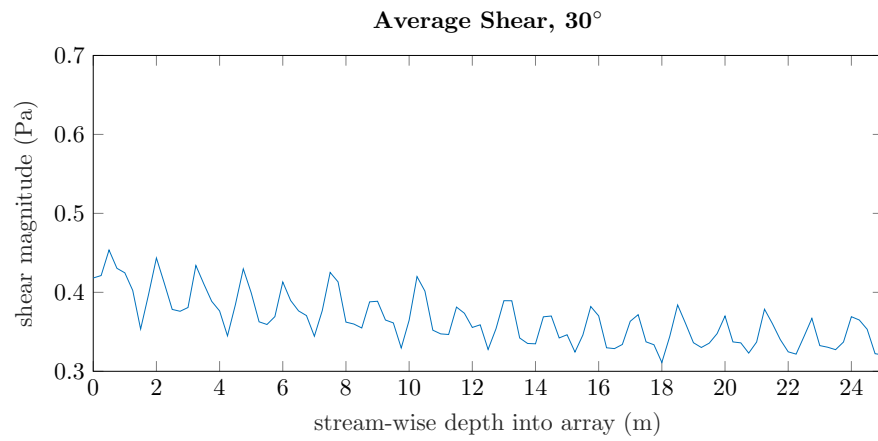
(b) Wind is nearly aligned with 26.5° corridors.

Average Shear, 70°
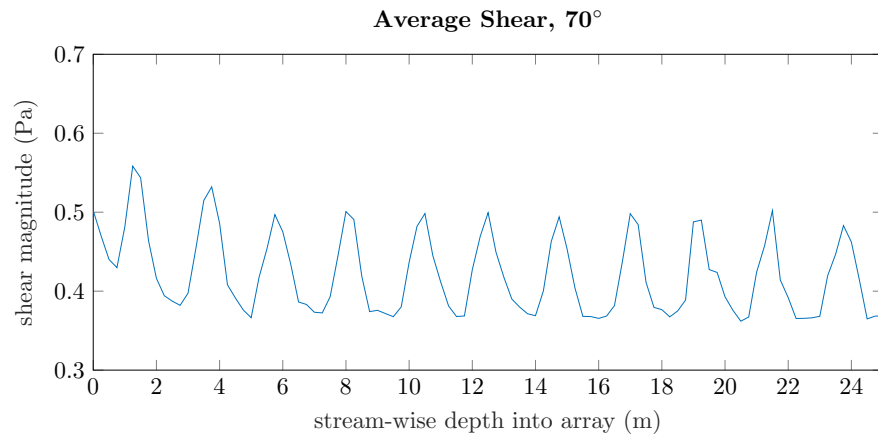
(c) Wind periodically encounters rows at a high angle with elements nearly aerodynamically aligned.

FIG. 7: Mean shear magnitude, computed by temporal and transverse wind direction averaging. The three angles encounter elements at different spatial frequencies, which are not representative of overall array effectiveness.

C.   Changes in shear for a single rotated box

Flow around a single element was investigated to understand the role of aerodynamics under a rotated wind field without the interaction of other objects. Figure 8 shows the mean and standard deviation of shear measured on the same sampling grid for the ten wind direction angles. Counter-intuitively, the average shear increases with frontal area, and the standard deviation decreases. Though the increase is modest, this shows that the aerodynamics of the roughness elements play a dominant role over frontal area. The cause of this phenomenon lies in the asymmetry of the roughness elements. Figure 9 shows binned surface shear for a single element rotated by $0°$ and $50°$. In the rotated case frontal area is larger. However, most of the wake shelter is behind the longer edge, as seen in fig. 9b. When the long edge of the box meets the wind profile head-on, there is a significant spreading of the shelter area, as shown in fig. 9a.

The histogram in fig. 10 was constructed to identify the shear magnitudes that account for the lack of shear reduction under rotations with the greatest frontal area. For all of the simulations, shear magnitude distributions were largely bimodal. However, for angles where large frontal areas are presented to the incoming flow, shear magnitude observed in the $0.1\,\text{Pa}$ to $0.3\,\text{Pa}$ range have a wider spread. This accounts for both the decrease in the element's ability shelter the surface on the lee side, and decrease in standard deviation.
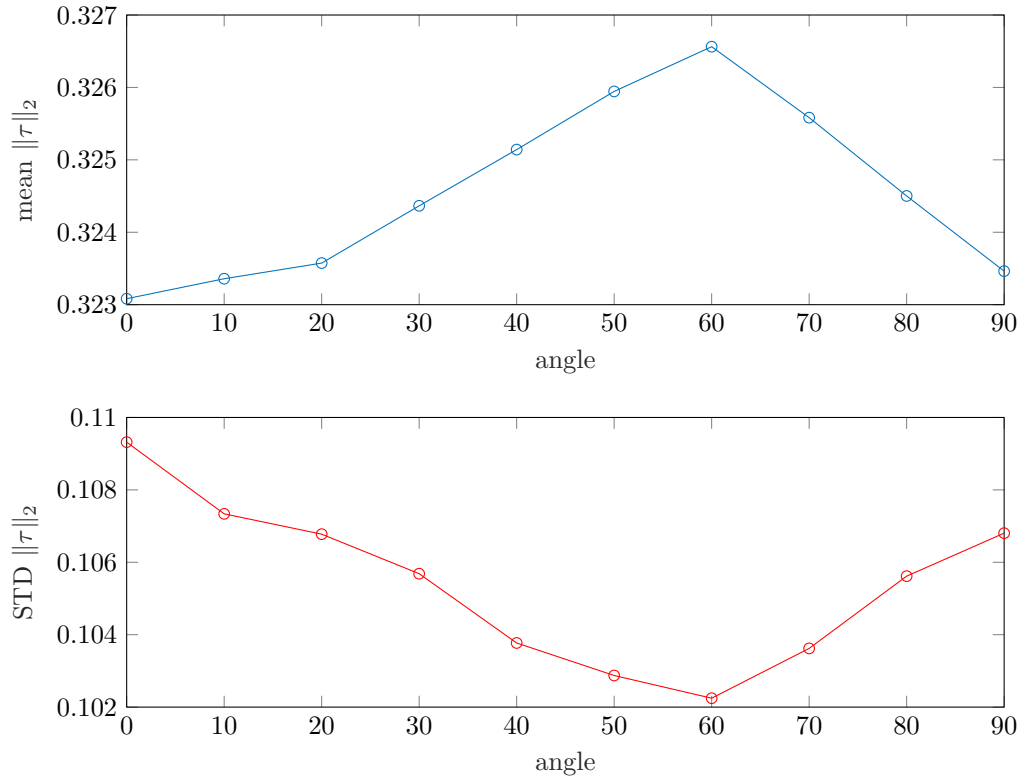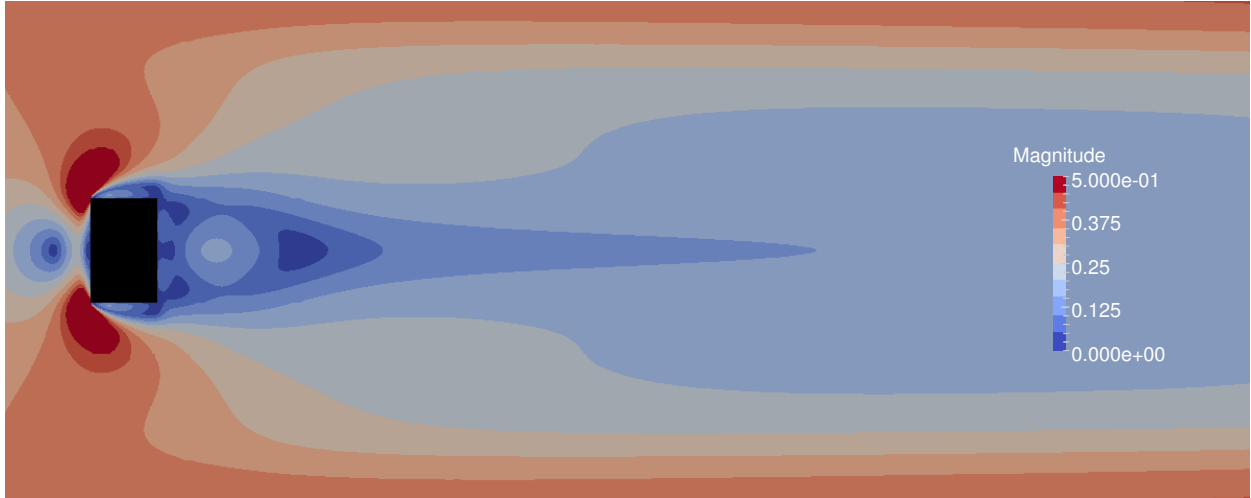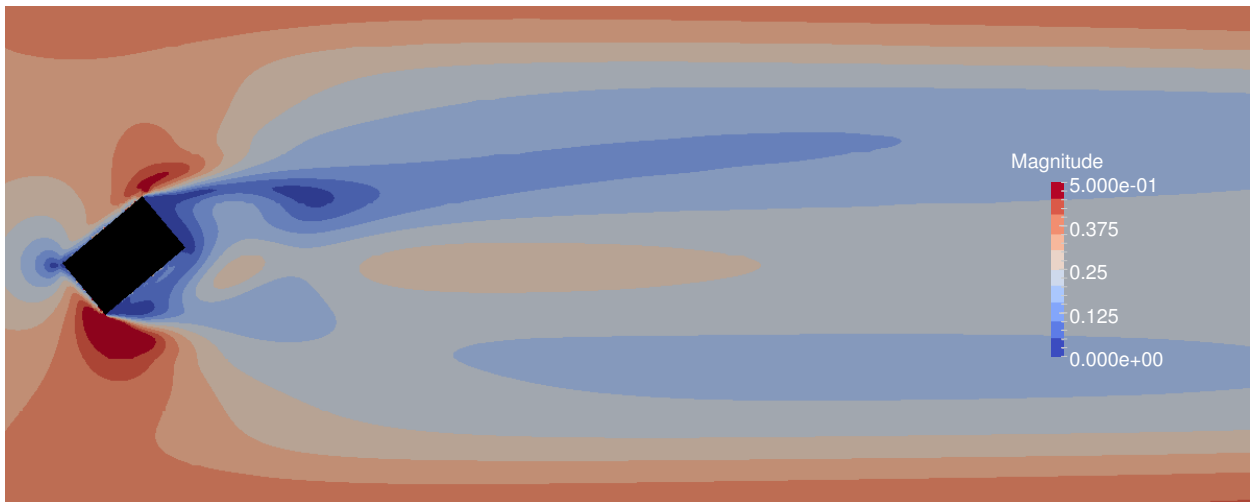
FIG. 8: Mean and standard deviation of temporally averaged sampled shear $\|\tau\|_2$ around the single rotated roughness element.

(a) Shear magnitude pattern for the element under a 0° rotation in the wind field.

(b) Shear magnitude pattern for the element under a 50° rotation in the wind field.

FIG. 9: Mean time-averaged shear patterns for two wind directions. Flow is from left to right.
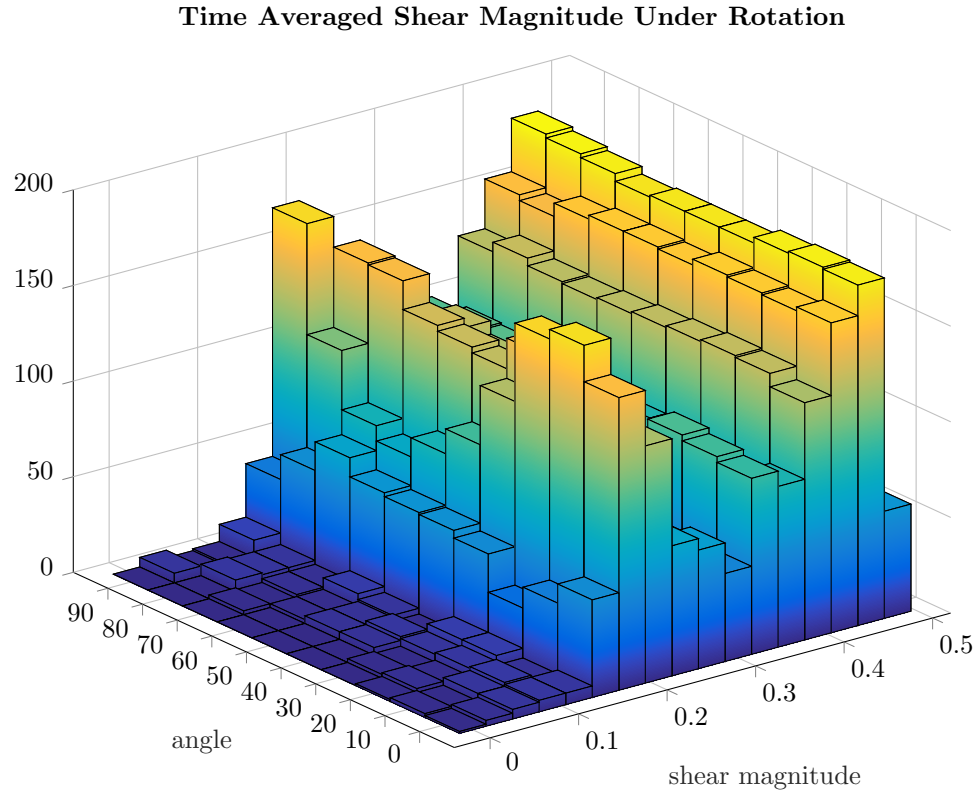
Time Averaged Shear Magnitude Under Rotation

FIG. 10: A histogram of shear magnitudes for different rotations of the single roughness element.

VI.   CONCLUDING REMARKS

Multi-angle simulations were conducted to determine the effectiveness of a roughness array in reducing ground shear. Simulations of the array corroborated field observations of rapid decreases in near-ground wind speeds upon entering the initial two rows of roughness elements. Additional simulations of a single rotated elements showed that frontal area is not a mechanistic parameter to use alone in predicting how roughness will affect the magnitude of shear stress reduction and the size or shape of the shelter zone. These results also suggest that element geometry needs to be considered when using roughness to modulate the surface shear stress for wind erosion control. Consideration needs to be given to the wind regime and the shape or orientation of elements to maximize their effectiveness to reduce surface shear stress. Flow visualization shows the upward deflection of the wind profile upon entering the roughness array is caused by strong vertical mixing around the elements.

ACKNOWLEDGMENT

[1] Andrew S. Goudie. Desert dust and human health disorders. *Environment International*, 63:101 – 113, 2014. ISSN 0160-4120. doi:http://dx.doi.org/10.1016/j.envint.2013.10.011. URL http://www.sciencedirect.com/science/article/pii/S0160412013002262.

[2] A. Cook, E. Derbyshire, and G. Plumlee. Impact of natural dusts on human health. In J.O. Nriagu, editor, *Encyclopedia of Environmental Health*, pages 178 – 186. Elsevier, Burlington, 2011. ISBN 978-0-444-52272-6. doi:https://doi.org/10.1016/B978-0-444-52272-6.00162-8. URL http://www.sciencedirect.com/science/article/pii/B9780444522726001628.

[3] N.J. Middleton. Desert dust hazards: A global review. *Aeolian Research*, 24:53 – 63, 2017. ISSN 1875-9637. doi:http://dx.doi.org/10.1016/j.aeolia.2016.12.001. URL http://www.sciencedirect.com/science/article/pii/S1875963716301215.

[4] J.A. Gillies. 11.4. fundamentals of aeolian sediment transport: Dust emissions and transport near surface. In John F. Shroder, editor, *Treatise on Geomorphology*, pages 43 – 63. Academic Press, San Diego, 2013. ISBN 978-0-08-088522-3. doi:http://dx.doi.org/10.1016/B978-0-12-374739-6.00297-9.

[5] J.A. Gillies, H. Green, G. McCarley-Holder, S. Grimm, C. Howard, N. Barbieri, D. Ono, and T. Schade. Using solid element roughness to control sand movement: Keeler dunes, keeler, california. *Aeolian Research*, 18:35 – 46, 2015. ISSN 1875-9637. doi:http://dx.doi.org/10.1016/j.aeolia.2015.05.004.

[6] Qingfang Jiang, Ming Liu, and James D. Doyle. Influence of mesoscale dynamics and turbulence on fine dust transport in owens valley. *Journal of Applied Meteorology & Climatology*, 50(1):20 – 38, 2011. ISSN 15588424.

[7] Tezz C. Niemeyer, Dale A. Gillette, John J. Deluisi, Young J. Kim, William F. Niemeyer, Trevor Ley, Thomas Gill, and Duane Ono. Optical depth, size distribution and flux of dust from owens lake, california. 24:463–479, 05 1999.

[8] Aya Hagishima, Jun Tanimoto, Koji Nagayama, and Sho Meno. Aerodynamic parameters of regular arrays of rectangular blocks with various geometries. 132:315–337, 08 2009.

[9] O. Coceal, A. Dobre, T. G. Thomas, and S. E. Belcher. Structure of turbulent flow over regular arrays of cubical roughness. *Journal of Fluid Mechanics*, 589:375409, Oct 2007. doi:10.1017/S002211200700794X.

[10] Charles J. Doolittle, Scott D. Drews, and David B. Goldstein. Near-field flow structures about subcritical surface roughness. *Physics of Fluids*, 26(12):124106, 2014. doi:10.1063/1.4903306. URL `http://dx.doi.org/10.1063/1.4903306`.

[11] M. K. A. Neophytou, C. N. Markides, and P. A. Fokaides. An experimental study of the flow through and over two dimensional rectangular roughness elements: Deductions for urban boundary layer parameterizations and exchange processes. *Physics of Fluids*, 26(8):086603, 2014. doi:10.1063/1.4892979. URL `http://dx.doi.org/10.1063/1.4892979`.

[12] Benjamin Walter, Christof Gromke, Katherine Leonard, Costantino Manes, and Michael Lehning. Spatio-temporal surface shear-stress variability in live plant canopies and cube arrays. 143, 05 2012.

[13] Jose Luis Santiago, Alberto Martilli, and Fernando Martín. Cfd simulation of airflow over a regular array of cubes. part i: Three-dimensional simulation of the flow and validation with wind-tunnel measurements. *Boundary-Layer Meteorology*, 122(3):609–634, Mar 2007. ISSN 1573-1472. doi:10.1007/s10546-006-9123-z. URL `https://doi.org/10.1007/s10546-006-9123-z`.

[14] Y. Cheng, F.S. Lien, E. Yee, and R. Sinclair. A comparison of large eddy simulations with a standard $\kappa - \epsilon$ reynolds-averaged navierstokes model for the prediction of a fully developed turbulent flow over a matrix of cubes. *Journal of Wind Engineering and Industrial Aerodynamics*, 91(11):1301 – 1328, 2003. ISSN 0167-6105. doi:http://dx.doi.org/10.1016/j.jweia.2003.08.001.

[15] Wai Chi Cheng and Fernando Porté-Agel. Adjustment of turbulent boundary-layer flow to idealized urban surfaces: A large-eddy simulation study. *Boundary-Layer Meteorology*, 155(2):249–270, May 2015. ISSN 1573-1472. doi:10.1007/s10546-015-0004-1. URL `https://doi.org/10.1007/s10546-015-0004-1`.

[16] Cheng Huang, Yan Bao, Dai Zhou, and Jin Quan Xu. Large eddy simulation for wind field analysis

based on stabilized finite element method. *Journal of Zhejiang University-SCIENCE A*, 12(4):278–290, 2011. ISSN 1862-1775. doi:10.1631/jzus.A1000114.

[17] Zheng Tong Xie, Omduth Coceal, and Ian P. Castro. Large-eddy simulation of flows over random urban-like obstacles. *Boundary-Layer Meteorology*, 129(1):1, Aug 2008. ISSN 1573-1472. doi:10.1007/s10546-008-9290-1. URL https://doi.org/10.1007/s10546-008-9290-1.

[18] Alexander Yakhot, Heping Liu, and Nikolay Nikitin. Turbulent flow around a wall-mounted cube: A direct numerical simulation. *International Journal of Heat & Fluid Flow*, 27(6):994 – 1009, 2006. ISSN 0142727X.

[19] Alberto Martilli and Jose Santiago. Cfd simulation of airflow over a regular array of cubes. part ii: Analysis of spatial average properties. 122:635–654, 01 2007.

[20] John A Gillies, William G Nickling, and James King. Shear stress partitioning in large patches of roughness in the atmospheric inertial sublayer. 122:367–396, 02 2007.

[21] Abulitipu Abulaiti, Reiji Kimura, and Yoshinori Kodama. Effect of flexible and rigid roughness elements on aeolian sand transport. *Arid Land Research & Management*, 31(2):111 – 124, 2017. ISSN 15324982. URL http://dist.lib.usu.edu/login?url=http://search.ebscohost.com/login.aspx?direct=true&db=aph&AN=121994480&site=eds-live.

[22] Nijs Jan Duijm. Estimates of roughness parameters for arrays of obstacles. *Boundary-Layer Meteorology*, 91(1):1–22, 1999. ISSN 1573-1472. doi:10.1023/A:1001794831176.

[23] Byung Gu Kim, Changhoon Lee, Seokjun Joo, Ki Cheol Ryu, Seogcheol Kim, Donghyun You, and Woo-Sup Shim. Estimation of roughness parameters within sparse urban-like obstacle arrays. *Boundary-Layer Meteorology*, 139(3):457–485, Jun 2011. ISSN 1573-1472. doi:10.1007/s10546-011-9590-8. URL https://doi.org/10.1007/s10546-011-9590-8.

[24] H. G. Weller, G. Tabor, H. Jasak, and C. Fureby. A tensorial approach to computational continuum mechanics using object-oriented techniques. *Computers in Physics*, 1998.

[25] F. Moukalled, L. Mangani, and M. Darwish. *The Finite Volume Method in Computational Fluid Dynamics*. 2015.

[26] D.M. Hargreaves and N.G. Wright. On the use of the k model in commercial {CFD} software to model the neutral atmospheric boundary layer. *Journal of Wind Engineering and Industrial Aerodynamics*, 95 (5):355 – 369, 2007. ISSN 0167-6105. doi:http://dx.doi.org/10.1016/j.jweia.2006.08.002.

[27] P.J. Richards and R.P. Hoxey. Appropriate boundary conditions for computational wind engineering models using the $\kappa - \epsilon$ turbulence model. In S. Murakami, editor, *Computational Wind Engineering 1*, pages 145 – 153. Elsevier, Oxford, 1993. ISBN 978-0-444-81688-7. doi:http://dx.doi.org/10.1016/B978-0-444-81688-7.50018-8.

A COMPARISON OF NUMERICAL AND ANALYTICAL INVESTIGATIONS OF

VISCOUS GRAVITY SPREADING IN A PARABOLIC FISSURE

A comparison of numerical and analytical investigations of viscous gravity spreading in a parabolic fissure

Eden Furtak-Cole

Utah State University, Department of Mathematics and Statistics, Logan, UT 84322

Aleksey Telyakovskiy

University of Nevada, Department of Mathematics and Statistics, Reno, NV 89557

(Dated: December 6, 2017)

We investigate the viscous free spreading of a constant volume of liquid in a fissure with a parabolic cross section. A 1D flow model is derived that can be solved with similarity variables and a variety of ODE methods. Governing assumptions are tested against a 3D Navier-Stokes two phase flow simulation. Comparisons of the analytical and computational profiles are presented. We also investigate the convergence of an arbitrary initial condition to the limiting similarity solution. Computational experiments are conducted for an initial condition generated from the 1D flow model, as well as an arbitrary mass conservative rectangular initial condition representing a physical experiment. Results show excellent agreement between the 1D flow model and the two-phase flow simulation. Differences in the observed flow model can be attributed to the presence of vertical motions and surface tension in the numerical simulations.

I. INTRODUCTION

Gravity currents occur in a variety of natural and industrial settings[1][2][3]. Viscous immiscible gravity currents are of particular interest, and can be studied in controlled lab experiments. Low dimensional flow models with analytical solutions offer an important class of benchmarks, but rely on a set of flow simplifications. Basic rheological studies are required to develop flow theory that can be upscaled for applications such as flow through fractured media.

A number of models have been developed for viscous gravity spreading, with a common application being flows through porous media. Potential flow models are one example with a rich history in both subsurface and general fluid flows. Analytical solutions of potential flow problems are often restricted to steady state processes on infinite domains. Polubarinova-Kochina[4] posed and solved many subsurface potential flow problems with conformal mappings. For time dependent applications, Longo et al.[5] took the approach of linearizing a potential flow system. An alternative approach to 2D potential flow equations is a reduction to 1D using the Dupuit-Forcheimer (DF) assumption[6]. This assumption restricts the velocity to the horizontal direction only, and velocity is calculated from the slope of the free surface. Implicit in this approach is that the velocity is depth-averaged and calculated using the gradient of the hydrostatic approximation of pressure. This results in a non-divergence free velocity field for incompressible fluids, with continuity imposed on the free surface[7]. For uniform permeability, these assumptions result in the Boussinesq equation with constant coefficients. This equation is commonly used in problems involving the spreading of unconfined groundwater, or flow between parallel plates[8–10]. Similarity solutions exist for a variety of initial and boundary conditions. For the free spreading of a finite volume of fluid, Barenblatt[11] constructed a solution using a point mass at an initial time. Using a symmetry argument, this solution can be applied to both boundary value and initial condition problems.

Domains with spatially variable permeability can be modeled using the generalized Boussinesq equations[12–15]. Similarity solutions exist for cases where the permeability takes the form of a power law in the horizontal or vertical directions. Hele-Shaw cells can be used to study these flows experimentally, with viscous drag being used as a proxy for permeability[16]. Positioning flat cell walls in a wedge configuration results in generalized Boussinesq equation that can be solved with with such an approach. Ciriello et al.[15] constructed similarity solutions to injection problems in horizonal and vertical wedge configurations. Zheng et al.[17] found solutions in a similar configuration for drainage from an initially full aquifer. Curved plates resulting in power-law permeability are difficult to manufacture, but have been used for horizontally oriented experiments

by Zheng et al. [18], as well as vertical experiments by Di Federico et al. [19].

Multiphase numerical modeling of the aforementioned experiments with the 3D Navier-Stokes equations is analogous to pore scale modeling, and to the authors knowledge have not yet been performed. Though the geometry is relatively simple, the aspect ratio requires a very large computation mesh to resolve the front in the directions transverse to the primary flow direction. The issue is further complicated by sharp mesh angles where wedge walls meet. Parabolic wedges provide an interesting geometry that lends itself to both analytical and 3D numerical simulations. We derive a flow model for viscous gravity spreading in a parabolic fissure using the DF assumption, resulting in a generalized Boussinesq type equation. We then investigate properties of the flow using a 3D two phase volume of fluid (VOF) Navier-Stokes equation (NSE) simulation. The availability of flow pathlines in the numerical simulation gives insight into the experimentally observed phenomenon of arbitrary initial conditions converging on the similarity solution. The inclusion of surface tension in the numerical simulation allows us to assess the accuracy of experiments in Hele-Shaw cells as compared to the 1D model.

II. GOVERNING EQUATIONS AND BOUNDARY CONDITIONS

A. 1D flow model

We derive a flow model for a viscous fluid in a parabolic fissure. Consider a fluid element formed by vertically cutting through a parabolic prism, as seen in Figure 1. Conservation of mass dictates that the rate of change of fluid in the elementary volume is equal to the difference in volumetric fluxes through the faces at y and $y + dy$:

$$
\frac{\partial}{\partial t} \left(\int_0^{h_v(y,t)} b(z)dzdy \right) = \left(\int_0^{h_v(y,t)} b(z)u_v(y,z,t)dz \right)
$$
$$
- \left(\int_0^{h_v(y+dy,t)} b(z)u_v(y+dy,z,t)dz \right), \tag{1}
$$

where the width of the wedge for height z is given by $b(z)$, u_v is the fluid speed in the y direction, and $h_v(y,t)$ is the height of the free surface. We consider only the flux of an incompressible high viscosity fluid (e.g. glycerol), neglecting the gaseous atmosphere being displaced. Neglecting the higher order terms of the Taylor expansion in the second term on the right hand side of (1), we
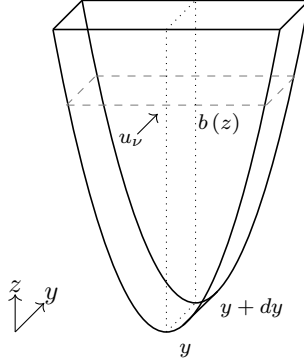
FIG. 1: A fluid element within the wedged Hele-Shaw cell. The cross-sectional width is denoted $b(z)$, and the flux through the element is u_ν.

obtain,

$$\frac{\partial}{\partial t}\left(\int_0^{h_v(y,t)} b(z)dzdy\right) = -\frac{\partial}{\partial y}\int_0^{h_v(y,t)} b(z)u_v(y,z,t)dzdy. \tag{2}$$

As seen in Figure 1, the parabolic cross section is oriented against gravity in the $x-z$ plane. The equation of the fissure walls in the $x-z$ plane is

$$z = \omega x^2 \tag{3}$$

for some constant $\omega > 0$. Then the distance between the walls as a function of height is,

$$b(z) = 2\sqrt{\frac{z}{\omega}}. \tag{4}$$

Under the assumption of Poiseuille flow between parallel plates for an arbitrary height given by $b(z)$, we obtain permeability as a power law function of height:

$$k(z) = \frac{(b(z))^2}{12} = \frac{z}{3\omega}. \tag{5}$$

This permeability results in the Darcy velocity,

$$u_v(y,z,t) = -\frac{z}{3\omega}\frac{\rho g}{\mu}\frac{\partial h_v(y,t)}{\partial y}. \tag{6}$$

Performing substitutions for width (4), Darcy velocity (6), and integrating (2) yields,

$$\frac{\partial}{\partial t}\left(\frac{4}{3\sqrt{\omega}}h_v^{\frac{3}{2}}\right) = \frac{\partial}{\partial y}\left(\frac{4}{15\sqrt{\omega^3}}\frac{\rho g}{\mu}h_v^{\frac{5}{2}}\frac{\partial h_v}{\partial y}\right), \tag{7}$$

which further simplifies to,

$$\frac{\partial}{\partial t}\left(h_v^{\frac{3}{2}}\right) = \frac{\rho g}{5\omega\mu}\frac{\partial}{\partial y}\left(h_v^{\frac{5}{2}}\frac{\partial h_v}{\partial y}\right). \tag{8}$$

We perform the change of variables, $\Upsilon = h^{\frac{3}{2}}$, to obtain a special form of the porous medium equation (PME)[7]:

$$\frac{\partial}{\partial t}\Upsilon = \frac{2\rho g}{35\omega\mu}\frac{\partial^2}{\partial y^2}\Upsilon^{\frac{7}{3}}.$$ (9)

We are interested in case of free spreading under the force of gravity, which results in the boundary condition[11],

$$\Upsilon(0,t) = \sigma t^{-\frac{1}{7/3+1}},$$ (10)

where $\sigma > 0$ for an initially empty fissure.

The problem defined by (9) and (10) can be solved by introducing the dimensionless similarity variables,

$$\xi = \frac{x(1+\beta(m-1))^{\frac{1}{2}}}{(a\sigma^{(m-1)}t^{1+\beta(m-1)})^{\frac{1}{2}}},$$ (11)

and

$$h = \sigma t^\beta H(\xi),$$ (12)

where $\xi(x,t)$ is the similarity variable, $H(\xi)$ is a scaling function, $m = 7/3$ nonlinear diffusion exponent in the PME, and $a = \frac{2\rho g}{35\omega\mu}$. The parameter β is the time exponent of the boundary condition, in this case $-\frac{1}{7/3+1}$. Substitution of the similarity variables results in the ordinary differential equation,

$$\frac{d^2 H^m(\xi)}{d\xi^2} + \frac{\xi}{2}\frac{dH(\xi)}{d\xi} - \lambda H(\xi) = 0,$$ (13)

where $\lambda = \frac{\alpha}{1+\alpha(m-1)}$, and $H(0) = 1$, $H(\xi_0) = 0$. The front position in terms of similarity variables is ξ_0, and is found in the process of solution. The "mathematician's pressure" change of variables[7]

$$H = u^{\frac{1}{m-1}}$$ (14)

performed on (13) produces an ODE with integer powers:

$$\frac{m}{m-1}u\frac{d^2u}{d\xi^2} + \frac{m}{m-1}\left(\frac{m}{m-1}-1\right)\left(\frac{du}{d\xi}\right)^2 + \frac{\xi}{2}\frac{1}{m-1}\frac{du}{d\xi} - \lambda u = 0.$$ (15)

Boundary conditions are given by,

$$u(0) = 1,$$ (16)

and

$$u(\xi_0) = 0. \tag{17}$$

The system (15)–(17) can be solved using a Runge-Kutta solver, or a power series of the form (Furtak-Cole et al 2018, submitted),

$$u(\xi) = \sum_{n=0}^{\infty} a_n \left(1 - \frac{\xi}{\xi_0}\right)^n. \tag{18}$$

B.   3D flow model

Flow through the parabolic fissure can be modeled with the incompressible 3D Navier-Stokes equations,

$$\rho \frac{D\mathbf{u}}{Dt} = -\nabla p + \rho \mathbf{g} + \mu \Delta \mathbf{u}, \tag{19}$$

and

$$\nabla \cdot \mathbf{u} = 0, \tag{20}$$

where ρ is density, $\mathbf{u}$ is velocity, p is pressure, μ viscosity, and $\mathbf{g}$ is the gravity vector. Phases are tracked using a VOF method[20]. The indicator function α takes on values in the range of $[0, 1]$ and can be interpreted as the fraction of two phase types within a computation cell. For our purposes, 0 denotes air, and 1 denotes glycerol. For any computational cell in the domain, the average fluid properties for density and viscosity are calculated by summing over the i phases,

$$\rho = \sum_i \rho_i \alpha_i \tag{21}$$

and

$$\mu = \sum_i \mu_i \alpha_i \tag{22}$$

respectively. The indicator function evolves under the equation,

$$\frac{\partial \alpha_i}{\partial t} + \nabla \cdot \mathbf{u}\alpha_i + \nabla \cdot \mathbf{u}_c \alpha_i (1 - \alpha_i) = 0, \tag{23}$$

where the counter gradient transport term $\nabla \cdot \mathbf{u}_c \alpha_i (1 - \alpha_i)$ acts as a limiter based on the maximum velocity $\mathbf{u_c}$ on interface. Surface tension effects are calculated by,

$$S = \gamma K \nabla \alpha, \tag{24}$$

where γ is the surface tension, and K is the curvature $-\nabla \cdot \mathbf{n}$. The term for S is added to the momentum equation (19) to obtain,

$$\rho \frac{D\mathbf{u}}{Dt} = -\nabla p + \rho \mathbf{g} + \mu \Delta \mathbf{u} + \gamma K \nabla \alpha. \tag{25}$$

We use the finite volume method toolbox openFOAM[2122] implementation interDyMFoam in all 3D flow simulations. A hexahedral base mesh was constructed with a $2 - 1 - 1$ aspect ratio. This mesh was fitted to a 3D parabolic geometry using the snappyHexMesh utility. The parabolic geometry was constructed to the specifications in section II C. Mesh adaptivity was set to refine two levels, based on the interface values of the indicator function α.

We supply boundary conditions to mimic a lab experiment, with a top open to the atmosphere. For velocity, a no-slip condition,

$$\mathbf{u} = 0, \tag{26}$$

is applied to all solid walls. To allow fluxes of air at the top of the experiment, a zero gradient,

$$\frac{\partial \mathbf{u}}{\partial \mathbf{n}} = 0, \tag{27}$$

condition is applied. A no-flow pressure condition is applied at the solid walls,

$$\frac{\partial p}{\partial \mathbf{n}} = 0. \tag{28}$$

At the top of the experiment, total pressure P_{tot} is calculated as,

$$p_{tot} = p_{atm} - .5\rho \|\mathbf{u}\|^2. \tag{29}$$

C.   Flow assumptions, initial conditions and parameter values

The 1D flow model uses the DF assumption, and does not include the effects of surface tension. The 3D model include the full velocity field and includes surface tension effects, but requires large amounts of computational power to solve. This is largely due to the aspect ratio of the domain, which requires very small finite volumes between the parabola walls. The parabolic geometry is defined by

$$z = 2000x^2, \tag{30}$$

extruded along the y axis for one meter. This corresponds to a gap of $2\,\mathrm{cm}$ at a maximum height of $0.2\,\mathrm{m}$.

parameter	value
σ	$0.06\,\mathrm{m}$
ρ	$1261\,\mathrm{kg\,m^{-3}}$
μ	$1.412\,\mathrm{Pa\,s}$
g	$9.8\,\mathrm{m\,s^{-2}}$
ω	2000

(a) 1D flow model.

parameter	value
γ	$0.0634\,\mathrm{N\,m^{-1}}$
ρ_{air}	$1\,\mathrm{kg\,m^{-3}}$
μ_{air}	$1.48 \times 10^{-5}\,\mathrm{Pa\,s}$
$\rho_{glycerol}$	$1261\,\mathrm{kg\,m^{-3}}$
$\mu_{glycerol}$	$1.412\,\mathrm{Pa\,s}$
g	$9.8\,\mathrm{m\,s^{-2}}$

(b) 3D flow model.

TABLE I: Parameter values for the 1D and 3D flow models. Density and viscosity are the same for the glycerol phase in both models.

An initial condition for the 3D simulation was chosen from the 1D analytical solution. The parameter values in table Ia were inserted into the 1D flow model. The resulting curve at time $t = 0.3\,\mathrm{s}$ was arbitrarily chosen as a suitable initial condition for a lab-scale experiment of the free spreading of a finite volume of glycerol.

III.   COMPUTATIONAL EXPERIMENTS

A.   Profile comparison

A comparison between the 3D simulation and 1D analytical solution is shown in fig. 2. Excellent agreement is observed between the two methods, both in propagation distance and shape. The poorest fit is seen in fig. 2a. At that time, the simulated front lags behind the analytical solution, and undercutting is observed at the bottom of the advancing front. At later times, the free surface of the 1D analytical solution lags behind the NSE simulation. We note that the 1D model does not include surface tension effects, while the 3D model does.

B.   Transition to similarity

The transition from initial conditions to late time similarity solutions has been investigated with physical experiments[18,23], and analytical solutions[24]. In both cases, the reason for late time convergence is difficult to understand mechanistically. To perform experiments, initial conditions that do not coincide with the similarity solution are often used out of necessity. Numerical experiments offer a previously unobtainable opportunity to compare the convergence of arbitrary initial
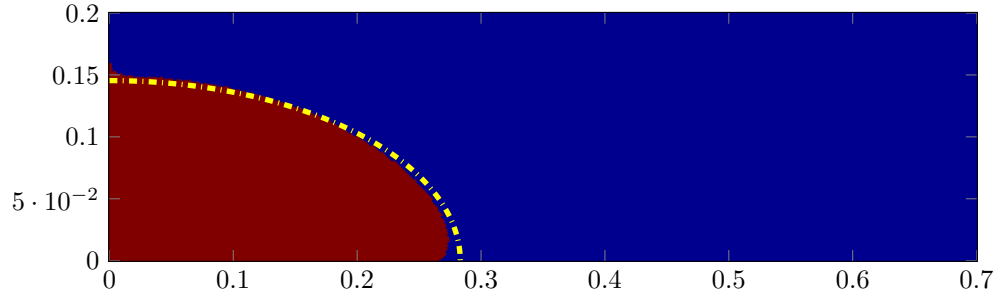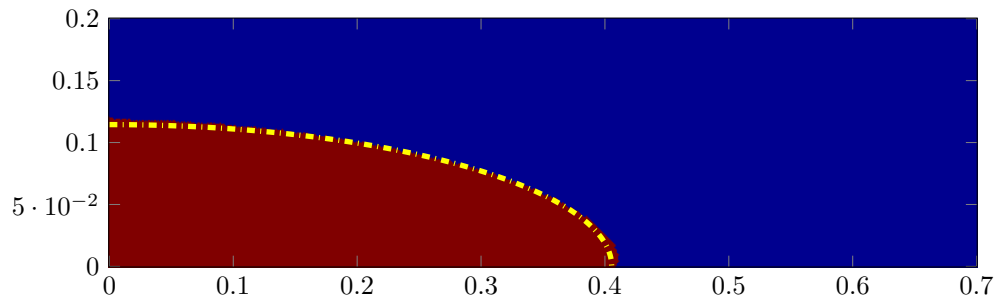
(a) 1.3 s
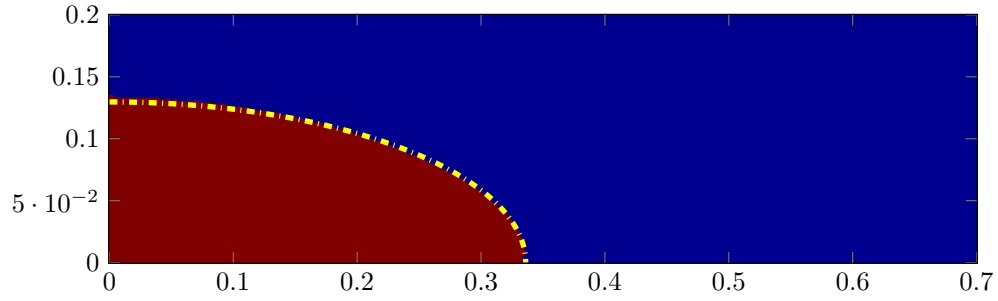
(b) 2.3 s
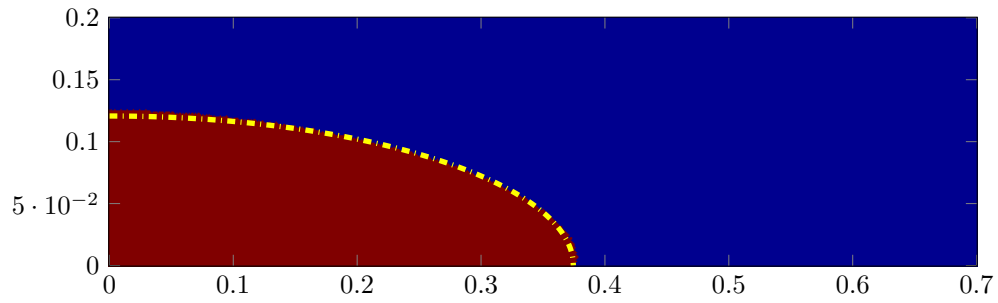
(c) 3.3 s

(d) 4.3 s

FIG. 2: Comparison between the NSE simulation and 1D flow model for four times. Red represents glycerol in the simulation results, the yellow dotted line is free surface from the 1D model. The analytical free surface at time $t = 0.3$ s was used as an initial condition for the NSE simulation. Horizontal and vertical lengths are in meters.

conditions. In the results presented in section III A, we observe the greatest discrepancy between the solutions at early times, though the simulation is started from the analytical curve. This is due to the inclusion of vertical motions and surface tension in the simulation.

A hypothetical mass-conserving initial condition of rectangular cross section was produced by solving,

$$\int_0^{y_1} \int_0^{z=.18} 2\sqrt{\frac{z}{2000}} dz dy = 3.425\,48 \times 10^{-4}, \tag{31}$$

where the upper limit $z = .18$ was chosen arbitrarily. The value for the right hand side was produced by numerically computing the volume integral defined by the analytically-derived initial condition from the 1D flow model in the parabolic geometry. For practical purposes, such an initial condition could be used in an experiment by setting a lock gate to hold the volume of glycerol at the initial time. Propagated distances versus time and residuals between the 3D simulation and 1D analytical solution front propagation are shown in fig. 3. As seen in fig. 3a, the rectangular analytical simulation rapidly converges to the simulation started with the analytical initial condition. Both simulations run ahead of the 1D solution for later times. This is likely due to the overall slow-down of the front, but continued surface tension action of the fluid at the base of the wedge.

Figure 3b shows that the differences produced by subtracting the analytical curves from the simulations go to zero as the two curves converge. Why this happens can not be determined from the analytical solution, as no known exact solution exists for the rectangular initial condition. Pathlines of tracer particles placed on the free surface of the rectangular initial condition reveal the rapid collapse of fluid furthest from the initial condition generated by the similarity solution. Figure 4 shows these pathlines, produced over 1 s of simulation time. Pathlines are colored by velocity, showing very high velocities are generated near the upper right corner of the initial condition.

C. Surface tension and vertical velocity

The similarity solution to the 1D flow problem is a weak solution that is a continuous function. By contrast, the interface resolved by the numerical simulations is double valued at the propagating edge. We track this behavior by measuring the height at which the flow overrides itself at the tip of the advancing front. The height of undercut is shown in fig. 5 as a function of time. The time $t = 2\,\text{s}$ is marked with a vertical line as the approximate time that the two numerical simulations reach the same propagation distance as the 1D solution (see fig. 3). This suggests that the slowing
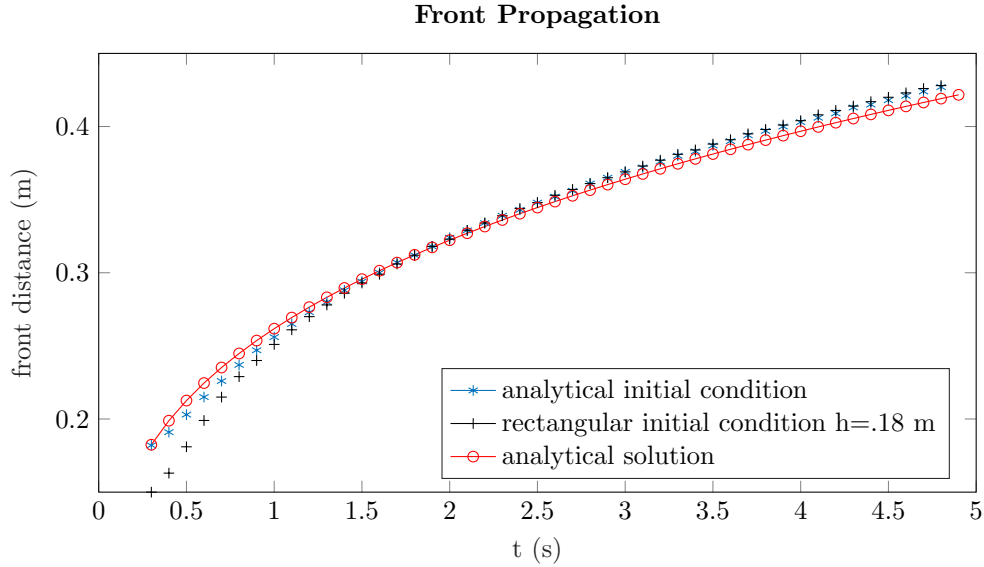
(a) Front propagation for the two simulations and 1D flow model.
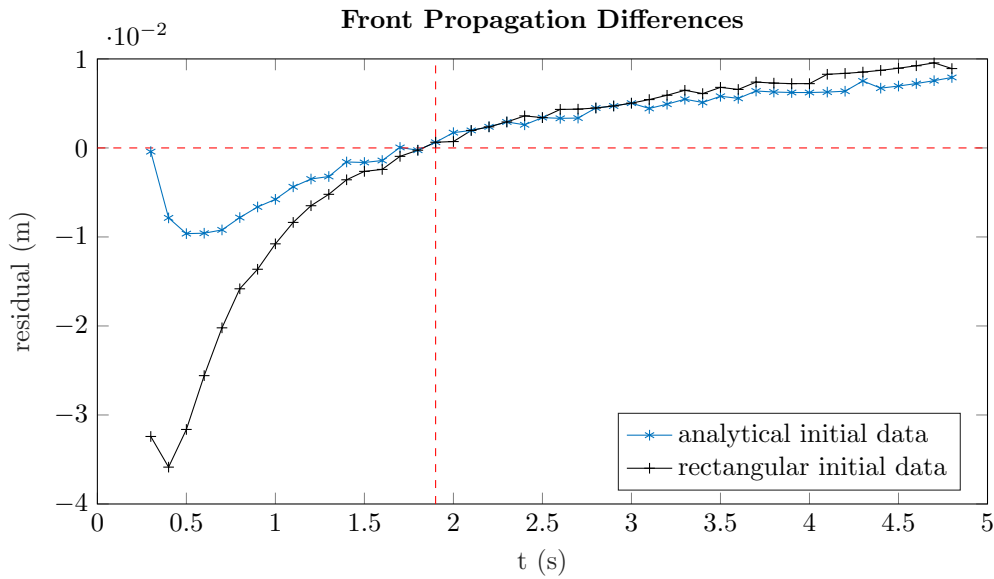
(b) Differences made by subtracting 1D flow model results from the simulations.

FIG. 3: Front propagation through time is shown for the two simulations and 1D flow model in 3a. Differencecs produced by subtracting the analytical solution from the simulations is shown in 3b. The three solutions align just before 2 s.

of front propagation is a mechanism for late time convergence. For early times, the fluid mass has enough pressure gradient to over-run the base of the parabola, where flow permeability tends to zero. At later times, the propagation speed of the front is slow enough that fluid can fill in the bottom of the parabola vertically.
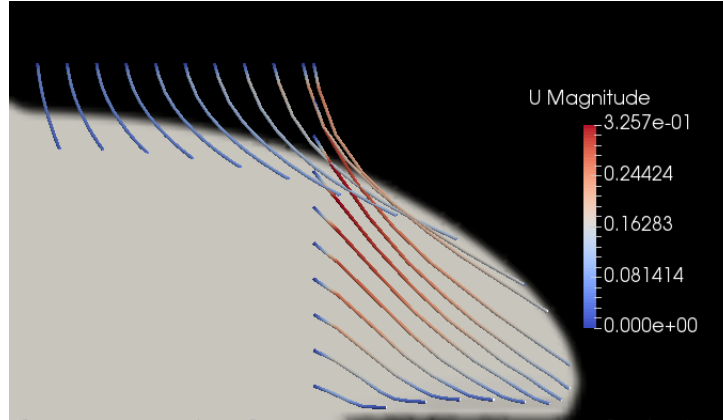
FIG. 4: Pathlines placed on the rectangular initial condition, carried forward 1 second in time. Pathlines are colored by velocity magnitude.
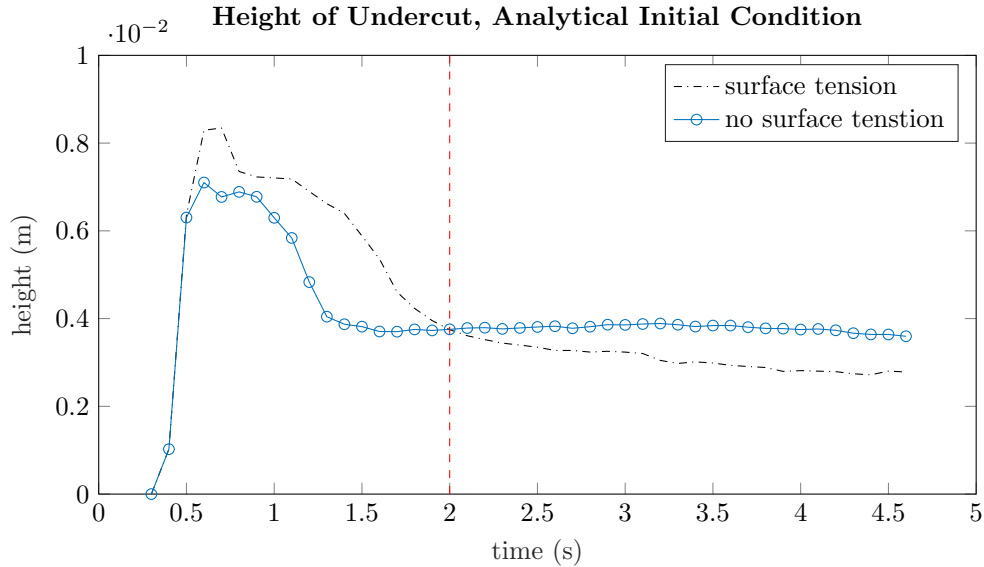

FIG. 5: Height of undercutting in the capillary zone as a function of time. The removal of surface tension results in a profile with less undercutting at early times. The time $t = 2\,\mathrm{s}$ is marked by a dotted line.

Undercutting for a surface tension free simulation is also given in fig. 5. Equilibrium is reached significantly earlier, and at a greater height. Concavity patterns remain nearly the same, indicating that this behavior is primarily driven by the vertical velocity that is not present in the 1D model. In the undercut region, surface tension acts parallel to the direction of front propagation, which could explain the height difference between the two simulations at late times.

IV. CONCLUDING REMARKS

A 1D flow model was solved with similarity variables and compared to numerical solutions to the NSE using the VOF method and mesh adaptivity in a 3D parabolic fissure. Excellent agreement was observed between the two models. It was demonstrated that an arbitrary initial condition is unstable, and attracts strongly to the late time solution for both models. Early time discrepancies between the two models are shown to be primarily due to the treatment of velocity in the two models. Surface tension plays a dominant role at later times, and shifts the time at which the flow reaches an equilibrium of height undercutting.

ACKNOWLEDGMENT

---

[1] Herbert Huppert. Gravity currents: A personal perspective. *Journal of Fluid Mechanics*, 554:299 – 322, 05 2006.

[2] M.J. Leahy, J. Ennis-King, J. Hammond, H.E. Huppert, and J. Neufeld. Application of gravity currents to the migration of co2 in heterogeneous saline formations. *Energy Procedia*, 1(1):3331 – 3338, 2009. ISSN 1876-6102. doi:https://doi.org/10.1016/j.egypro.2009.02.120. URL `http://www.sciencedirect.com/science/article/pii/S1876610209007632`. Greenhouse Gas Control Technologies 9.

[3] J E Simpson. Gravity currents in the laboratory, atmosphere, and ocean. *Annual Review of Fluid Mechanics*, 14:213–234, 11 1982.

[4] P.Y. Polubarinova-Kochina. *Theory of Groundwater Movement*. Princeton University Press, 1962.

[5] Sandro Longo, Valentina Ciriello, Luca Chiapponi, and Vittorio Di Federico. Combined effect of rheology and confining boundaries on spreading of gravity currents in porous media. *Advances in Water Resources*, 79:140 – 152, 2015. ISSN 0309-1708. doi:http://dx.doi.org/10.1016/j.advwatres.2015.02.016. URL `http://www.sciencedirect.com/science/article/pii/S0309170815000482`.

[6] David B McWhorter and Daniel K. Sunada. *Ground-Water Hydrology and Hydraulics*. Water Resources Publications, 1977.

[7] Juan Luis Vazquez. *The Porous Medium Equation, Mathematical Theory*. Oxford University Press, 2007.

[8] D.A Lockington, J.-Y Parlange, M.B Parlange, and J Selker. Similarity solution of the Boussinesq equation. *Advances in Water Resources*, 23(7):725 – 729, 2000. ISSN 0309-1708. doi:http://dx.doi.org/10.1016/S0309-1708(00)00004-X. URL `http://www.sciencedirect.com/science/`

article/pii/S030917080000004X.

[9] Aleksey S. Telyakovskiy, Gasto A. Braga, Satoko Kurita, and Jeff Mortensen. On a power series solution to the Boussinesq equation. *Advances in Water Resources*, 33(9):1128 – 1129, 2010. ISSN 0309-1708. doi:http://dx.doi.org/10.1016/j.advwatres.2010.06.017. URL http://www.sciencedirect.com/science/article/pii/S0309170810001296.

[10] David E. Rupp and John S. Selker. Drainage of a horizontal Boussinesq aquifer with a power law hydraulic conductivity profile. *Water Resources Research*, 41(11), 2005. ISSN 1944-7973. doi:10.1029/2005WR004241.

[11] G I. Barenblatt. *Scaling*. Cambridge University Press, 2003.

[12] G I. Barenblatt. On some unsteady-state movements of liquid and gas in porous medium. *Prikl. Mat. i Mekh.*, 16(1):67–78, 1952.

[13] G I. Barenblatt. On some problems of unsteady filtration (in russian). *Izv. AN SSSR*, (6):97–110, 1954.

[14] Jeffrey S. Olsen and Aleksey S. Telyakovskiy. Polynomial approximate solutions of a generalized Boussinesq equation. *Water Resources Research*, 49(5):3049–3053, 2013. ISSN 1944-7973. doi:10.1002/wrcr.20242. URL http://dx.doi.org/10.1002/wrcr.20242.

[15] Valentina Ciriello, Sandro Longo, Luca Chiapponi, and Vittorio Di Federico. Porous gravity currents: A survey to determine the joint influence of fluid rheology and variations of medium properties. *Advances in Water Resources*, 92:105 – 115, 2016. ISSN 0309-1708. doi:http://dx.doi.org/10.1016/j.advwatres.2016.03.021. URL http://www.sciencedirect.com/science/article/pii/S0309170816300835.

[16] Rainer Helmig. *Multiphase Flow and Transport Processes in the Subsurface*. Springer, 1997.

[17] Zhong Zheng, Beatrice Soh, Herbert E. Huppert, and Howard A. Stone. Fluid drainage from the edge of a porous reservoir. *Journal of Fluid Mechanics*, 718:558568, 2013. doi:10.1017/jfm.2012.630.

[18] Zhong Zheng, Ivan Christov, and Howard A. Stone. Influence of heterogeneity on second-kind self-similar solutions for viscous gravity currents. 747, 04 2014.

[19] V. Di Federico, S. Longo, Stuart King, L. Chiapponi, D. Petrolo, and V. Ciriello. Gravity-driven flow of herschel–bulkley fluid in a fracture and in a 2d porous medium. *Journal of Fluid Mechanics*, 821:59–84, 6 2017. ISSN 0022-1120. doi:10.1017/jfm.2017.234.

[20] C.W Hirt and B.D Nichols. Volume of fluid (vof) method for the dynamics of free boundaries. *Journal of Computational Physics*, 39(1):201 – 225, 1981. ISSN 0021-9991. doi:https://doi.org/10.1016/0021-9991(81)90145-5. URL http://www.sciencedirect.com/science/article/pii/0021999181901455.

[21] F. Moukalled, L. Mangani, and M. Darwish. *The Finite Volume Method in Computational Fluid Dynamics*. 2015.

[22] H. G. Weller, G. Tabor, H. Jasak, and C. Fureby. A tensorial approach to computational continuum mechanics using object-oriented techniques. *Computers in Physics*, 1998.

[23] Herbert E. Huppert and Andrew W. Woods. Gravity-driven flows in porous layers. *Journal of Fluid Mechanics*, 292:5569, 1995. doi:10.1017/S0022112095001431.

[24] Marc Hesse, Hamdi Tchelepi, B. J. Cantwel, and F M. Orr Jr. Gravity currents in horizontal porous layers: Transition from early to late self-similarity. *Journal of Fluid Mechanics*, 577:363 – 383, 04 2007.

CONCLUSION

The importance of fluid dynamics in the natural environment can not be overstated. A diverse approach is needed to develop numerically-tractable models of fluid flow, examine flows around anthropogenic structures, and continue the development rheological theory. A solution procedure was developed for potential flow in the subsurface, which can be applied to landscape-scale problems in two or three spatial dimensions. We observed a great computational savings by limiting the implicit part of the solver to the saturated zone. Additionally, explicit front tracking, handling of merging interfaces, and a relaxation of the CFL condition were achieved. Existing CFD techniques were used to study the influence of wind direction on erosion control roughness arrays. Simulations agreed with measured and qualitative flow characteristics. Shear reduction was quantified, and insight was gained into the roughness array's mechanism of action. Single element simulations revealed strong effects of aerodynamics, and suggest that the current body of research on roughness calculations requires further development. A 1D model was derived for viscous flow in a parabolic fissure, and compared to two-phase flow simulations. Excellent agreement was observed. The use of numerical simulations allow for the isolation of flow effects that would not be achievable in a laboratory setting. Differences in the early and late time results was mechanistically explained and will be useful in the future development of physical experiments.

CURRICULUM VITAE

Eden Furtak-Cole

Utah State University

Department of Mathematics and Statistics   Phone: (415) 754-5091

Animal Science Building   Email: `furtak@aggiemail.usu.edu`

Logan, UT 84322, USA

Education

Ph.D. Applied and Interdisciplinary Mathematics, Utah State University, Dec. 2017

M.S. Mathematics, University of Nevada-Reno, 2013

B.S. Applied Mathematics, University of Vermont, 2008

B.A. Geography, University of Vermont, 2008

Current Research Projects

Assessing the shear reduction behavior of erosion control roughness arrays using computational fluid dynamics techniques.

Developing an efficient and novel solution procedure to the subsurface potential flow equations using a fast marching method.

Using the Navier-Stokes equations and Dupuit-Forchiemer approximated similarity solutions to explore the early time behavior of viscous gravity spreading in parabolic fissures.

Publications

Journal Articles

Furtak-Cole, E., Telyakovskiy, A. S., and Cooper, C. A. (2017). A Series Solution for Horizontal Infiltration in an Initially Dry Aquifer, Advances in Water Resources (under review)

Gillies, J. A., Nickling, W. G., Tilson, M., **Furtak-Cole, E.** (2012). Wind-formed Gravel Bed Forms, Wright Valley, Antarctica, J. Geophys. Res.-Earth Surface, 117, (F4), F04017, Online, doi: 10.1029/2012JF002378

Book Chapters

Dupigny-Giroux, L.-A. and **Furtak-Cole, E.** "Multiangular imaging of wetlands in new England," in Wetland: Ecology, Conservation and Restoration, Frank Columbus (editor), Nova Science Publishers, Inc., pp. 7-14.

Presentations

Furtak-Cole, E. (2017). "A numerical method for potential flow in the subsurface." poster presented at the SIAM Pacific Northwest Conference, Corvallis, Oregon.

Furtak-Cole, E. (2017). "A fast marching method for the porous medium equation." poster presented at the Western PDE Conference, Provo, Utah.

Furtak-Cole, E. , A. S. Telyakovskiy, and C. A. Cooper, (2016). "A series solution for horizontal infiltration in an initially dry aquifer." Paper presented at the American Mathematical Society sectionals, Denver, Colorado.

Furtak-Cole, E. and Telyakovskiy A. S.,(2014). "A series solution to the porous medium equation." American Geophysical Union, December 2014 (pos.

Gillies, J. A., Nield, J., Nickling, W. G., **Furtak-Cole, E.** (2013). Testing shelter index and a simple wind speed parameter to characterize vegetation control of sand transport threshold and flux, Paper presented at the European Geophysical Union General Assembly: Vienna, Austria, April 7, 2013

Hiscox, A.L., M. Rudnicki, H-B Su, A. Finger and **E. Furtak-Cole**, (2011). "Persistence of turbulence in and above a forest canopy." Poster presented at the IUFRO Wind and Trees Conference, Athens, GA

Hiscox, A.L, H. Thistle and **E. Furtak-Cole**, (2011). "Lidar derived mixing heights for dispersion modeling." Paper presented at the American Association of Geographers Annual Meeting, Seattle, Washington.

Finger, A., **E. Furtak-Cole**, A.L.Hiscox, M. Rudnicki and H.B. Su, (2010). "Turbulence stationarity within a forest canopy." Poster presented at the 29th Conference on Agricultural and Forest Meteorology, Keystone, Colorado.

Technical Reports

Gillies, J.A. and **E. Furtak-Cole** (2012). Using Plants to Control Sand Movement and Dust Emissions. Report prepared for Great Basin Unified Air Pollution Control District, Bishop CA, September 2012.

Employment

Research Assistant, Desert Research Institute, 2011–2013.

Instructor, University of Nevada, Reno, SU2015, SU2017.

Research Assistant, Louisiana State University, 2008–2009.

High Performance Computing Experience

Utah Center For High Performance Computing, SLURM scheduler, openFOAM.

Minnesota Supercomputer Institute, PBS scheduler, openFOAM.

Programming Languages and Skills

OpenFOAM advanced training certified (ESI)

Matlab, Julia, Linux/bash, Latex typesetting

Field Work

Belle Plaine, MN; Minnesota river acoustic Doppler current profiler bed scans and velocity transect profiling (2016).

Owens Lake, CA; experimental sediment stabilization array deployment (2014).

Jornada Experimental Range, NM; saltation monitoring instrument deployment (2012).

Green Mountain National Forest, VT; forest metrics for remote sensing calibration (2008).

White Mountain National Forest, NH; Snow water equivalent sampling (2007).

Green Mountain National Forest, VT; watershed field camp (2006).

Lab Work

Desert Research Institute

Conducted sloped aquifer flow simulation (2016).

Conducted porous media flow simulation (2013-2015).

Designed and constructed a wedged Hele-Shaw cell experiment (2012).

Louisiana State University

Performed atmospheric LIDAR maintenance (2009).

Funding Awards

Travel funding, Society for Industrial and Applied Mathematics sectional meeting, 2017.

Dissertation Fellowship, USU, $8000 2017-2018.

Travel funding, American Mathematical Society sectional meeting, 2016.

UNR Mathematics department lab funding, $200, 2012.

Leadership Experience

Vice president of USU student chapter 2016-2017.

Organized a workshop for the student research use of computing clusters. Presentations were given by experts from the Utah Center for High Performance Computing. (2016)

Teaching

Calculus III; SP 2016

Calculus II; SU 2014, FA 2011 (TA), SP 2012 (TA)

Calculus I; SU 2015, SP 2011 (TA)

Precalculus; SU 2012

Remedial Algebra; SU 2017

College Algebra; FA 2010 (TA)

Skills

Rescue diver, rescue climber, swift-water rescue

Small boat sailor, backcountry skier

Societies

Society for Industrial and Applied Mathematics (SIAM)

American Mathematical Society (AMS)

American Geophysical Union (AGU)

Gamma Theta Upsilon Geographic Honors Society (GTU)